NOVA SCHOOL OF SCIENCE & TECHNOLOGY

DEPARTAMENT OF MATERIAL SCIENCES

JOÃO AGOSTINHO GREGÓRIO DOS SANTOS

BSc in Micro and Nanotechnology

Ultrathin electronic tattoos (e-tattoo) for on-skin sensing

MASTER IN MICRO AND NANOTECHNOLOGY

NOVA University Lisbon

March, 2022

NOVA SCHOOL OF SCIENCE & TECHNOLOGY

DEPARTAMENT OF MATERIAL SCIENCES

Ultrathin electronic tattoos (e-tattoo) for on-skin sensing

JOÃO AGOSTINHO GREGÓRIO DOS SANTOS

Master/BSc in Micro and Nanotechnology

Adviser: Dr. Rui Igreja
Assintant Professor, NOVA University Lisbon

Examination Committee:

Chair: Dr. Rodrigo Martins,
Full professor in Materials Science Department, FCT NOVA

Rapporteurs: Dr. Carlos Dias
Assistant Professor, FCT NOVA

Adviser: Dr. Rui Igreja
Assintant professor, FCT NOVA

NOVA University Lisbon
March, 2022

Ultrathin electronic tattoos (e-tattoo) for on-skin sensing

ACKNOWLEDGMENTS

In first place, I'd like show gratitude to FCT-UNL, in particular the Department of Materials Sciences, and all the staff, who made my college experience so rich and eventful.

To my supervisor, professor Rui Igreja, a great *thank you* for the help and guidance, that allowed me, through a lot of ups and downs, to have a sensational MSC thesis experience.

To all the staff, investigators, and everyone in CENIMATIi3N and CEMOP, thank you for the help and patience integrating me in the laboratory! A special thank you to Alexandra Gonçalves, who continuously helped me find everything in needed for my work. An additional acknowledgment to professors Rita Branquinho and Joana Pinto, for all the help with a lot of analysis, and for the availability in clearing all my doubts.

An exceptional *thank you* needs to be said to Cátia Figueiredo, for all the help, patience, availability and for all the laughs during my work (a special emphasis on her patience), that made it so, that without her help, I would have been continuously lost in my work and couldn't have done half of what I did!

A very special *thank you* is also due to Ana Santa, Maria Morais and Emanuel Carlos for the help in teaching me how to operate equipment, and in clearing every doubt I could possibly have had in my work! To my college friends, Rui, André, Pedro, Raquel and Sergio that spent this journey with me, sharing experiences, laughs and the occasional "francesinha". You helped make my experience the best possible. To Nuno, for the car rides and all the help during my years in college, an enormous *thank you*!

To my São Bernardino friends, specifically Bruno and Bernardo, my oldest friends, a great *thank you.* A special thanks goes to Francisca who helped me so much with her artistic talent, who definitely helped make my work prettier!

Finally, to my family, mainly my parents and my amazing brother Francisco, who is always there for me, for the continuous support and belief during this adventure, a huge *thank you*!

“You miss 100% of the shots you don´t take "(Wayne Gretzky).

ABSTRACT

Wearable devices, specifically noninvasive attached on skin, provide a very versatile mean of acquiring physiological information about the human body, such as humidity, pH, heartbeat (electrocardiograms) and temperature, as well as are capable of transdermal stimulation and therapeutics. A key challenge in wearable devices, consist in a mismatch between the soft, curvilinear and dynamic skin, and the rigid and fragile silicon wafer-based electronics. Normally, the interfaces between skin and devices are insecure and can severally limit the functionality of the wearable devices, as well as increase the amount of motion artifacts and signal to noise ratio. Temporary electronic tattoos (e-tattoos) are an attractive platform for fabricating skin worn and body compliant wearable devices. These e-tattoos allow wearable sensors to mimic the structure of the skin, and conform very well when attached, due to its elasticity properties, while maintaining good sensing performances.

In this project, we explore the versatility and advantages of using different polymeric membranes, such as polyimides and parylene for the fabrication of temporary e-tattoos with sensing devices. Additionally, as a proof of concept, we fabricated a wearable and skin conformal e-tattoo for temperature sensing. The produced polyimide with aluminum sensors presented resistances of 49.5 Ω and 114.4 Ω and TCR values of 0.0017 $ºC^{-1}$ for both sensors. The polyimide with gold sensors achieved resistance values of 61.4 Ω and 142.3 Ω with TCR values of 0.0015 $ºC^{-1}$ and 0.0017 $ºC^{-1}$. The parylene with gold sensor presented a resistance of 26.4 Ω and TCR of 0.0015 $ºC^{-1}$.

Keywords: temporary e-tattoos, polyimide, parylene, temperature sensors

RESUMO

Dispositivos vestíveis, especificamente não-invasivos em contacto com a pele, apresentam um método bastante versátil para adquirir informação fisiológica sobre o corpo humano, tal como, humidade, pH, ritmo cardíaco e temperatura, e são também capazes de estimulação e terapia através da pele. Um dos maiores desafios destes dispositivos está na diferença entre a pele, suave e curvilínea, e a eletrónica baseada em bolachas, rígida e frágil. Normalmente, as interfaces entre pele e dispositivo são inseguras e podem limitar seriamente a funcionalidade do dispositivo, bem como podem aumentar os artefactos de movimento e o ratio sinal-ruído.

Tatuagens eletrónicas temporárias são uma plataforma atrativa para o fabrico de dispositivos vestíveis conformáveis à pele. Estas "e-tattoos" permitem ao sensor imitar a estrutura da pele, e conformam-se muito bem quando coladas à pele, devido às suas propriedades elásticas, mantendo boas performances sensoriais.

Neste projeto, exploramos a versatilidade e vantagens do uso de diferentes membranas poliméricas, nomeadamente poliamida e parileno, para o fabrico de e-tattoos. Adicionalmente, com o uso destas membranas, provámos que é possível fabricar uma tatuagem vestível e conformal, especificamente para sensor de temperatura. Os sensores de poliamida com aluminio apresentam resistências de 49,5 Ω e 114,4 Ω e valores de TCR de 0,0017 $ºC^{-1}$ para ambos. OS sensores de poliamida com ouro apresentam resistências de 61,4 e 142,3 Ω com valores de TCR de 0,0015 $ºC^{-1}$ e 0,0017 $ºC^{-1}$. O sensor de parileno com ouro apresentou uma resistência de 26,41 Ω e TCR de 0,0015 $ºC^{-1}$.

Palavras chave: tatuagens eletrónicas temporárias, poliamida, parileno, sensores de temperatura

CONTENTS

1 INTRODUCTION 1

1.1 Electronic tattoos (e-tattoos) 1

1.2 Polyimide 4

1.3 Parylene 5

1.4 Temperature sensors 6

2 MATERIALS AND METHODS 7

2.1 Production of the polyimide and parylene membranes 7

2.2 Aluminum and Titanium/Gold deposition 9

2.3 Characterization of the polyimide and parylene membranes 9

2.4 E-tattoo assembling and sensor characterization 10

3 RESULTS AND DISCUSSION 12

3.1 Characterization of parylene and polyimide membranes 12

3.1.1 FTIR analysis 12

3.1.2 Differential Scanning Calorimetry analysis 14

3.1.3 X-ray diffraction 17

3.2 Dimensioning and production of the e-tattoos 21

3.2.1 E-tattoo assembling 21

3.2.1 Sheet Resistance of the metalized membranes 23

3.3 Electrical characterization of the temperature sensors 24

3.3.1 Sensor´s nominal resistance 24
3.3.2 TCR calculation for the temperature sensor 27
4 CONCLUSION AND FUTURE PERSPECTIVES 32
5 33
6 ANNEXES 37
Annex I. Surface treatment of the membranes 37
Annex II. Cutting trials 38
Annex III. Determination of the theoretical resistance of the sensors 40
Annex IV. Determination of TCR with sample cooling 42
Annex V. On-skin Measurements 44

LIST OF FIGURES

Figure 1.1 — Different temporary tattoos currently developed to measure different human body information: a) electrochemical sensors based on printable temporary transfer tattoos [9]; b) graphene electronic tattoo sensors; [10]. c) Chest-Laminated Ultrathin and Stretchable E-Tattoo for the Measurement of ECG, SCG, and Cardiac Time Intervals [12]; d) Modular and Reconfigurable Wireless E-Tattoos for Personalized Sensing [13]. 3
Figure 1.2 — Different applications of polyimide polymers in sensors: a) polyimide based humidity sensor [26]; b) polyimide based force sensor [27] 4
Figure 1.3 - a) Parylene based device for memory and temperature sensing [31]; b) Flexible parylene-based wearable patch for ECG, EMG monitoring [32]..... 5
Figure 1.4 - a) Temperature sensor with flexible polyimide substrate [38]; b) parylene based thermal flow sensing array [39]..... 6
Figure 2.1 - Schematics of the fabrication of the polyimide membranes. a) spin coating of the PVA in a glass substrate; b) soft baking for 10 min at 110 ºC; c) spin coating of the adhesion promoter; d) spin coating of the polyimide; e) soft baking of the polyimide at 90 ºC and 150 ºC each for 90 s; f) curing at a ramp of 240 ºC/h from 150 ºC to 350 ºC, for 1 h and 20 min.... 8
Figure 2.2 - a) removal of the glass substrate in a heated plaque at 90 ºC for a continuous period of time; b) laminating the metalized membranes onto the tattoo paper. c) cutting process on a silhouette cutter plotter of the desired circuit..... 10
Figure 3.1 - ATR-FTIR spectrum of the parylene dimer and membranes. 13
Figure 3.2 - ATR-FTIR spectrum of the polyimide membranes..... 14
Figure 3.3 - DSC analysis of the tattoo paper; a) DSC peaks; b) Mass change during heating. 15
Figure 3.4 - DSC analysis of the parylene membranes; a) DSC peaks; b) Mass change during heating..... 15

Figure 3.5 - DSC analysis of the commercial Kapton membranes; a) DSC peaks; b) Mass change during heating; and of the polyimide membranes: c) DSC peaks; d) Mass change during heating.....16
Figure 3.6 - XRD diffractogram of the parylene membranes. 17
Figure 3.7 - XRD diffractogram of the parylene membranes with a 100 nm layer of aluminium. 18
Figure 3.8 - XRD diffractogram of the parylene membranes with an 80 nm layer of gold.....18
Figure 3.9 - XRD diffractogram of the polyimide membranes (6 µm). 19
Figure 3.10 - XRD diffractogram of the polyimide membranes with a 100 nm layer of aluminium. 20
Figure 3.11 - XRD diffractogram of the parylene membranes with a 80 nm layer of gold.....20
Figure 3.12 - E-tattoo assembling, full process: a) membrane production; b) metallization of the polymer membrane; c) peel-off of the metalized membrane; d) removal of the liner of the tattoo paper; e) sliding of the peeled-off membranes onto the tattoo paper; f) cutting of the circuit; g) application of the tattoo in the skin. 21
Figure 3.13 - Produced temperature sensing e-tattoos; a) PI_Al A (polyimide and aluminium); b) PI_Au A (polyimide and gold); Par_Au (parylene and gold). 22
Figure 3.14 - Produced sensors for the more complex circuit design; a) PI_Au B (polyimide and gold); b) PI_Al B (polyimide and aluminium).....22
Figure 3.15 - Analysis of the IV curve for sensor PI_Al A. 25
Figure 3.16 - Analysis of the IV curve for sensor PI_Au A. 25
Figure 3.17 - Analysis of the IV curve for sensor Par_Au. 26
Figure 3.18 - Analysis of the IV curve for sensor PI_Au B. 26
Figure 3.19 - Analysis of the IV curve for sensor PI_Al B. 27
Figure 3.20 - Sensor PI_Al A: a) Resistance variation with temperature increase; b) TCR curve. 28
Figure 3.21 - Sensor PI_Au A: a) Resistance variation with temperature increase; b) TCR curve. 28
Figure 3.22 - Sensor Par_Au: a) Resistance variation with temperature increase; b) TCR curve. 29
Figure 3.23 - Sensor PI_Au B: a) Resistance variation with temperature increase; b) TCR curve. 29
Figure 3.24 - Sensor PI_Al B: a) Resistance variation with temperature increase; b) TCR curve for the heating of the sample; c) TCR curve for the cooling of the sample. 30

Figure 6.1 - Membranes after thermal evaporation: a) without dry etching treatment; b) with dry etching surface treatment. 37
Figure 6.2 - Schematics of the subdivision of the designed sensors in 0.2 mm squares: a) simpler design; b) sensor with more complex design. 40
Figure 6.3 - TCR curve for the PI_Al A sensor, during cooling of the sample. 42
Figure 6.4 - TCR curve for the PI_Au A sensor, during cooling of the sample. 42
Figure 6.5 - TCR curve for the Par_Au sensor, during cooling of the sample. 43
Figure 6.6 - TCR curve for the PI_Au B sensor, during cooling of the sample. 43
Figure 6.7 - Measurements while on the tattoo paper: a) preparation of the sample; b) measurement of resistance to confirm the integrity of the circuit. 44
Figure 6.8 - a) Attachment of the circuit to the human skin and wetting of the tattoo paper; b) removal of the tattoo paper, leaving only the desired circuit on-skin. 45
Figure 6.9 - Measurements of resistance, while the sensor is attached on-skin. 45

List of Tables

Table 1 - Overview of different aplications of several types of e-tattoos. 4
Table 2 - Notable bands in the parylene films FTIR spectrum [41] 12
Table 3 - Frequencies of characteristic bands of the polyimide FTIR spectrum [43]. 14
Table 4 - Overview of the design and constitution of the tested sensors. 22
Table 5 - Voltage measurements for aluminium layers. 23
Table 6 - Voltage measurements for gold layers; 24
Table 7 - TCR values for Aluminum and Gold [50]; 27
Table 8 - Overview of the obtained values of R_s, R and TCR for the tested sensors. 31
Table 9 - Cutting trials for the polyimide and Al, and Ti/Au membranes. 38
Table 10 - Cutting trials for the parylene and Al, and Ti/Au membranes. 39

Acronyms and Symbols

Al	aluminum
Au	gold
CEMOP	center of Excellence in Microelectronics and Optoelectronics Processes
CENIMAT	centro de Investigação de materiais
DSC	differential scanning calorimetry
FTIR	Fourier transform infrared
PI	Polyimide
PVA	Polyvinyl Alcohol
TCR	temperature coefficient of resistance
rpm	rotations per minute
Ti	Titanium
TG	thermogravimetry

XRD	X-ray diffraction analysis
I	current
V	voltage
R	resistance
R_s	sheet resistance
Ω	ohm
min	minute
s	second
ρ	resistivity

1

INTRODUCTION

1.1 Electronic tattoos (e-tattoos)

Wearable sensors have received a major recent attention owing to their considerable promise for monitoring a wearers health [1].

E-tattoos are ultra-thin and ultra-soft electronics, sensors, and actuators, whose stiffness and mass density match well with those of human epidermis [2]–[4]. These sensors could be attached onto the skin by van der Waals interactions alone in a manner that does not irritate the skin during prolong use. The epidermal electronic system is almost mechanically unnoticeable to the carrier, and could retain conformal contact with the skin under compression/tension [5]. The softness and conformability offer several unique advantages over conventional thick and stiff sensors [6]. Firstly, conformable contact enlarges the contact area between the sensors and the skin, which can effectively lower the contact impedance and facilitate signal transfer across the sensor–skin interface. Second, when skin deforms, e-tattoos would be able to follow skin displacement, minimizing interfacial slippage and as a result, motion artifacts [7][8]

Figure 1.1a) depicts a temporary tattoo based electrochemical sensor for physiological analysis and environmental monitoring obtained by printing active ink materials such as carbon and Ag/AgCl on tattoo papers to obtain sensor electrodes with for epidermal chemical sensing and physiological monitoring [9]. In comparison, figure 1.1b) shows a stretchable and transparent graphene Tattoo (GET) sensor that is sub-micrometers in thickness and can be used to measure to measure electrocardiogram (ECG), electromyogram (EMG), electroencephalogram (EEG), skin temperature, and skin hydration. The GET is fabricated by a simple ”wet transfer" (copper-etching step, which ensures high continuity of the large-area graphene grown on copper foil), and "dry patterning” (the application of a programmable mechanical cutter plotter to carve out

the designed shapes on the graphene sheet) without requiring skin preparation or skin adhesive [10] [11]. In figure 1.1c) a chest laminated ultrathin and stretchable e-tattoo is shown that consists of a hair thin, skin soft, and highly stretchable PVDF vibration sensor for high fidelity SCG (Seismocardiogram) and ECG (Electrocardiogram) monitoring [12]. Now, in figure 1.1d) an e-tattoo can be viewed, that consists of: a generic near field communication (NFC) layer for wireless power and data transmission, a replaceable functional circuit layer for signal read-out, and an optional disposable gold (Au) electrode layer for ECG or hydration sensing [13]. Table 1 presents an overview of recent developments in wearable sensors, and e-tattoos. to attest to the versatility of these types of sensors.

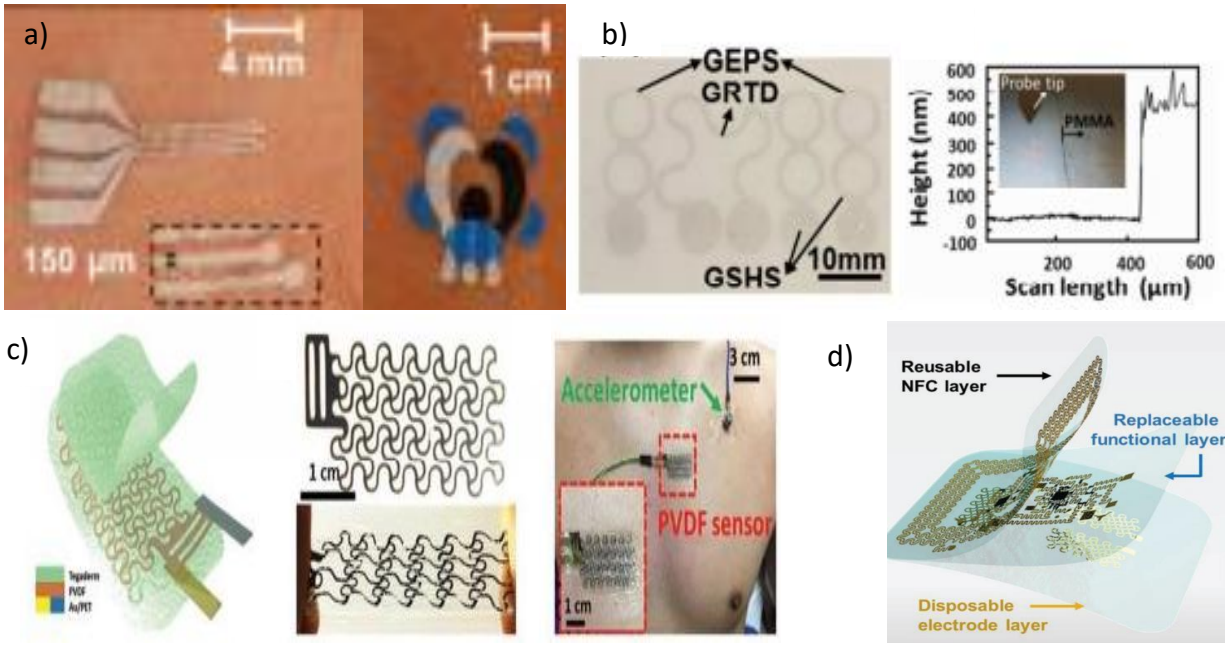

Figure 1.1 — Different temporary tattoos currently developed to measure different human body information: a) electrochemical sensors based on printable temporary transfer tattoos [9]; b) graphene electronic tattoo sensors; [10]. c) Chest-Laminated Ultrathin and Stretchable E-Tattoo for the Measurement of ECG, SCG, and Cardiac Time Intervals [12]; d) Modular and Reconfigurable Wireless E-Tattoos for Personalized Sensing [13].

Table 1 - Overview of different applications of several types of e-tattoos.

E-tattoo	Constituents	Function/Measures	Reference
Printable electrochemical sensors	Ag/AgCl	Epidermal and physio-logical sensing	[9]
Graphene electronic tattoo sensors	Graphene and Cu	ECG, skin temperature and skin hydration	[10]
Chest-Laminated Ultrathin and Stretch-able E-Tattoo	PVDF and Au	ECG, SCG, and Cardiac Time Intervals	[12]
Modular and Reconfigurable Wireless E-Tattoos	Tegaderm tape and Au	ECG or hydration sensing	[13]
Ultrasensitive mechanical crack-based sensor	Platinum thin film	Strain sensing	[14]
A flexible and highly pressure-sensitive sponge	Graphene and polyurethane	Pressure sensing	[15]
Iontronic microdroplet array	Indium-tin-oxide (ITO) and PET	Ultrasensitive tactile sensing	[16]

1.2 Polyimide

Polyimide (PI) is a high-performance polymer that has superior properties such as temperature stability, resistance to solvents and mechanical strength [17]. These polyamide (PI) films have remarkable optical properties (transparency and low solar absorption and infrared emission), high thermal stability and wide service temperature (−300–+300 °C), radiation resistance, enhanced electrical insulation, low density, toughness, flexibility, and high mechanical stability [18]–[22]. The dipole–dipole interactions between carbonyl bonds in the imide structure of macromolecules and charge transfer increases the mechanical and chemical stability of PIs.
PIs are suitable for coating applications due to adhesion to the several substrates such as metals, polymers, carbon, silica-based materials. Different coating methods such as solution-coating, dip-coating [23] or spin-coating [24][25] can be used to make thin membranes.

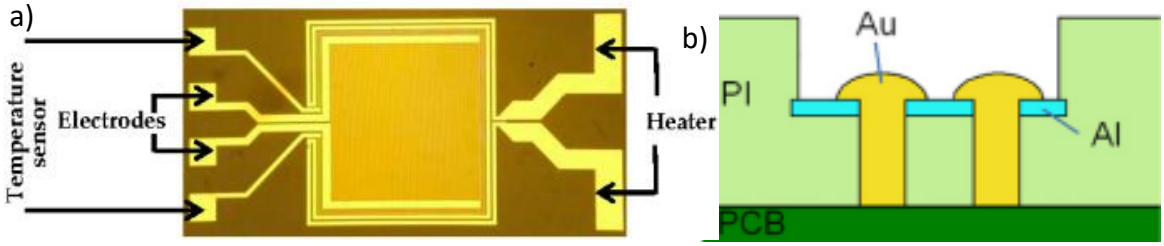

Figure 1.2 — Different applications of polyimide polymers in sensors: a) polyimide based humidity sensor [26]; b) polyimide based force sensor [27] .

Due to all these properties and versatility, polyimide membranes are ideal for the fabrication of wearable sensors. In figure 1.2 a), Boudaden et al. [26] reported a polyimide-based capacitive humidity sensor. This sensor consists of a transducer, in this case a pair of planar interdigitated electrodes (TiW and Au) and a polyimide sensitive layer for relative humidity measurements. In comparison, Jagoda et al. [27] developed flexible polyimide-based force sensor, illustrated in figure 1.3b). Polyimide is used in both as flexible substrate and as elastic dielectric between two levels of finger-shaped aluminum electrodes, to provide great force sensitivity.

1.3 Parylene

Parylene polymers are classified as thermoplastic polymers formed on substrate surfaces using vacuum deposition polymerization. Parylene possesses exceptional properties such as being stress free, truly conformal, chemical inertness, biocompatibility, present high dielectric strength, and optical transparency [28][29]. These types of polymers have ideal properties for barrier applications as their uniform deposition process allows for optimal coverage for encapsulation, making them widely used in biomedical applications such as coatings for medical implants [30]. Parylene, being a bio-friendly material as was previously refereed, shows the prominent capability of being safely used within the human body which makes it suitable for wearable device applications.

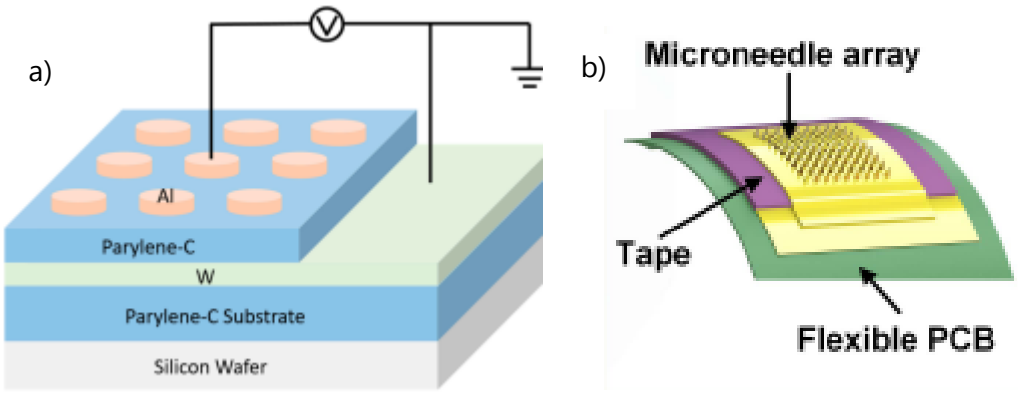

Figure 1.3 - a) Parylene based device for memory and temperature sensing [31]; b) Flexible parylene-based wearable patch for ECG, EMG monitoring [32].

Lin et al. [31] demonstrated a polymer (organic) device based on parylene-C with functionalities of memory and temperature sensing. The polymer device has a metal/polymer/metal (MIM), with Al top electrodes and W bottom electrodes in between parylene layers as shown in figure 1.3a). Meanwhile, In figure 1.3b), Huang, et al. [32] reported a flexible wearable patch integrating parylene-based microneedle array (MNA) and signal acquisition flexible PCB (FPC) circuit for long-term biopotential monitoring, namely electromyogram (EMG), electrocardiogram (ECG) measurements with high wearability and high applicability on any site of the body.

1.4 Temperature sensors

Body surface temperature is easily affected by the surrounding environment, bringing challenges to body temperature monitoring equipment [33]. The temperature sensors in e-skin are based on resistance thermometers, p–n junctions or composite materials undergoing thermal expansion [34]–[37].

Recently developed temperature sensors, specifically thin film thermocouples, have shown a small heat capacity and fast temperature measuring response time. One example of these sensors consists of a temperature-sensitive layer of platinum and indium oxide as the positive and negative electrodes, and a flexible substrate, in this case polyimide. This flexible temperature sensor has good deformation resistance and stability when measuring surfaces with different curvatures, and its illustrated in figure 1.4a) [38]. Meanwhile in figure 1.4b), is depicted a biocompatible parylene thermal flow sensing array. This device comprises several thin film platinum sensing elements sandwiched in a Parylene C membrane that is suspended over a bulk-micromachined silicon channel for improved thermal isolation for multi-mode testing in hot-film, calorimetric and low overheat ratios [39].

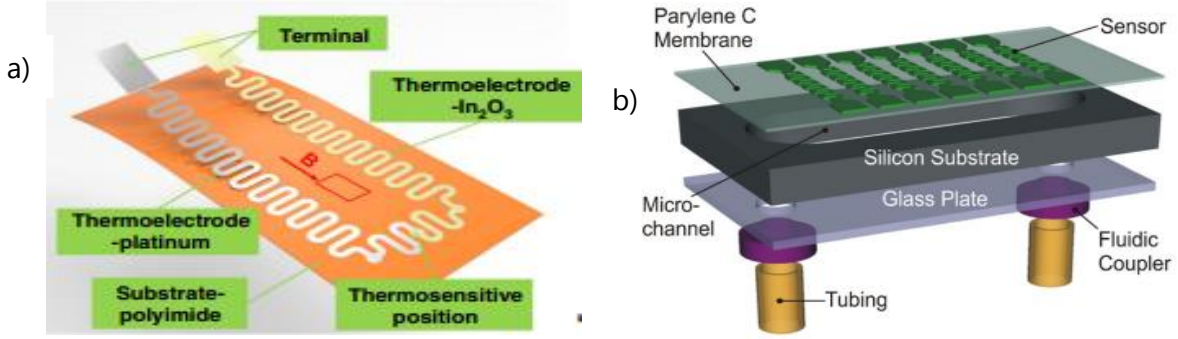

Figure 1.4 - a) Temperature sensor with flexible polyimide substrate [38]; b) parylene based thermal flow sensing array [39].

2

MATERIALS AND METHODS

2.1 Production of the polyimide and parylene membranes

The production of the polyimide membranes began with the mix of 5 g of PVA powder (88% hydrolyzed, average M.W. 20000-30000, Acros Organics) in 100 ml of DI-water (5wt%) in a glass flask heated at 90ºC with 1000 rpm until the dissolution was complete (approximately 12 hours). The glass substrates (Glass plates from Marienfeld) were cleaned in ultrasounds bath, firstly 10 min in acetone, followed by 10 minutes in isopropyl alcohol (IPA). Then the glass was cleaned with ultrapure water, and dried under N_2 jetting. The PVA solution, previously prepared and cooled for 3 hours at room temperature, was then spin-coated in a glass substrate (previously cleaned) using a syringe (10mL Injekt Luer Lock Solo from Braun) and a particle filter (0.45 µm PTFE filter from Chromafil). The spin coating conditions for the PVA were, 10 s at 1000 rpm with acceleration of 500 rpm/s, followed by 20 s at 2000 rpm with 1000 rpm/s of acceleration. After the spin coating, the sample was heated in a hot plaque for 10 min at 110 ºC. Following the PVA deposition, the adhesion promoter (VM652 from HD MicroSystems) was spin coated in the substrate and the spin coating conditions were: 30 s at 3000 rpm with 2000 rpm/ s acceleration. Polyimide (2611 from HD MicroSystems) was then spread onto the substrate with the PVA and adhesion promoter, and a thickness of 6µm was obtained with the following spin conditions: 7 s at 500 rpm (acceleration 500 rpm/s) and 30 s at 3000 rpm (acceleration 500 rpm/s). All the spin coating depositions were performed under clean room environment and vacuum conditions. The sample with the spin coated polyimides was soft baked at 90ºC for 90 seconds and at 150 ºC for 90 s. After the soft baking process, the samples were left cooling for

10 minutes, before the cure process, in which the samples were heated with a ramp of 240 ºC/h from 150 ºC to 350 ºC, and stayed at 350 ºC during 30 minutes, making a total curing time of 1 hour and 20 minutes, a process fully illustrated in figure 2.1.

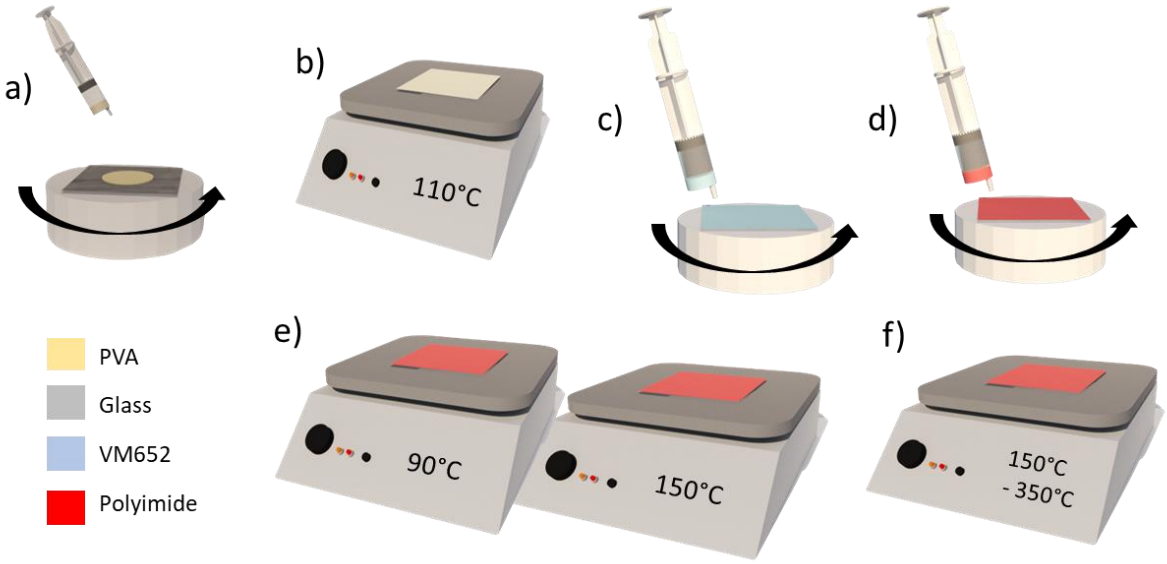

Figure 2.1 - Schematics of the fabrication of the polyimide membranes. a) spin coating of the PVA in a glass substrate; b) soft baking for 10 min at 110 ºC; c) spin coating of the adhesion promoter; d) spin coating of the polyimide; e) soft baking of the polyimide at 90 ºC and 150 ºC each for 90 s; f) curing at a ramp of 240 ºC/h from 150 ºC to 350 ºC, for 1 h and 20 min.

The parylene membranes were produced by CVD (chemical vapor deposition). The glass substrates were prepared equally to the polyimide procedure. After the cleaning of the substrates, a syringe (10 mL Injekt Luer Lock Solo from Braun) and a particle filter (0.45 µm PTFE filter from Chromafil) were used to place the PVA solution onto the substrates. The spinning conditions of the PVA are similar to the process of polyimide deposition, which are 10 s at 1000 rpm with 500 rpm/s acceleration, followed by 20 s at 2000 rpm with 1000 rpm/s acceleration. After the spin coating, the glass with the spin coated PVA was heated for 10 min at 110ºC. The CVD process begins with the weighing of 10 g of Parylene dimer, that was placed in aluminum foil and inside the chamber, that needs to reach a vacuum of 10 mbar for the deposition. As the chamber reaches the PLA of 10 mbar, the temperature was turned on, in the furnace and chamber, until their setpoint, 690 ºC and 135 ºC respectively, was reached. As the temperatures setpoint is reached, the vaporizer temperature is increased, while maintaining an 18 mbar (chamber pressure setpoint) pressure in the chamber, to deposit a 6µm thick layer of parylene in all the samples in the chamber.

2.2 Aluminum and Titanium/Gold deposition

After the production of the parylene and polyimide membranes, a metallization of the former was performed. By thermal evaporation, 100 nm of aluminum were deposited, and through e-beam assisted thermal evaporation, 6 nm of Titanium and 80 nm of Gold were deposited. For the thermal evaporation, the membrane was set in the chamber of the thermal evaporator, as a W crucible was filled with aluminum. The chamber was then left for 12 hours in vacuum. When the vacuum was at least $6.5x10^{-7}$ mbar, a current of 55 mA was applied in the crucible, in order to melt the aluminum, and the former was deposited in the substrate.

To deposit the Ti/Au alloy onto the polyimide and parylene substrates a e-beam assisted thermal evaporation process was used. A loaded gold crucible and titanium crucible, as well as 4 glass samples with the membranes already prepared were set in the chamber and left for 3 hours until a pressure of $3.0x10^{-6}$ mbar was reached in the chamber. The electron beam was then set onto the crucible with a current of 0.06 mA until the Titanium was melted and until the deposition of 6 nm of Titanium. The electron beam was then set onto the crucible with the gold, with a current of 0.05 mA, to melt the gold, and a layer of 80 nm was deposited in the sample. The initial temperature of the chamber was 20 ºC and the final was 32 ºC. The final pressure was $9.0x10^{-6}$ mbar.

2.3 Characterization of the polyimide and parylene membranes

In order to characterize the parylene and polyimide membranes, an ATR (Attenuated total reflectance) FTIR (Fourier transform infrared spectroscopy) analysis was performed from $600cm^{-1}$ to $3300\ cm^{-1}$ on a Nicolet 6700 FT-IR (from Thermo electron corporation) in order to determinate the chemical composition of the produced membranes. A Differential Scanning Calorimetry and Thermogravimetry (DSC-TG) analysis was performed in equipment STA 449F3 Jupiter on the membranes and the tattoo paper (Laser Tattoo A4-Paper from FOREVER) to evaluate their behavior with a temperature change, as well as to determine the temperature on which membrane degradation begins, and mass loss during sample heating. The measurements were taken from 27 ºC to 550 °C at 5 °C/min under ambient conditions.

Additionally, the membranes with and without the deposited metal, were analyzed in aP-ANalytical X´Pert PRO XRD (x-ray diffraction) diffractor, in the 2θ range from 0° to 90°, with a 0.1º step, in order to confirm the correct metallization of the membranes with the Ti/Au and Aluminum layers.

2.4 E-tattoo assembling and sensor characterization

The e-tattoo assembling began with the peeling off of the metalized membranes with Al or Ti/Au from the glass substrate. The samples were put in water at 90 ºC during 2 hours, to dissolve the PVA layer, thus peeling of the metalized membrane from de glass substrate. This process was followed by the slight wetting of the tattoo paper, in order to remove the liner, and to allow the metalized membrane to adhere to the paper. With both of these steps prepared the removed metalized polyimide and parylene membranes were then slide into the tattoo paper and then dried for 5 minutes in a hot plate at 55 ºC followed by 3 hours at room temperature. Finally, the sample, that needs to be fully dried, was cut by a Silhouette Cameo 4, with the desired Adobe Illustrator circuit for a temperature sensor and with the machine specifications being: blade 2; force 4; velocity 1 and repetitions 0 for the polyimide membranes and, blade 2; force 3; velocity 1 and repetitions 0 for the parylene membranes, as shown in figure 2.2. After the cutting of the serpentine shaped circuit design, the paper was then slightly wet again, in order to facilitate the peel-off of the extraneous parts of the membrane, leaving only the desired circuit on the tattoo paper. To attach the final sensor (to measure temperature) to the human skin, the skin surface was slightly wetted, and the tattoo paper was placed. Following this, the tattoo paper is then fully wetted and then its slide to keep only the desired circuit.

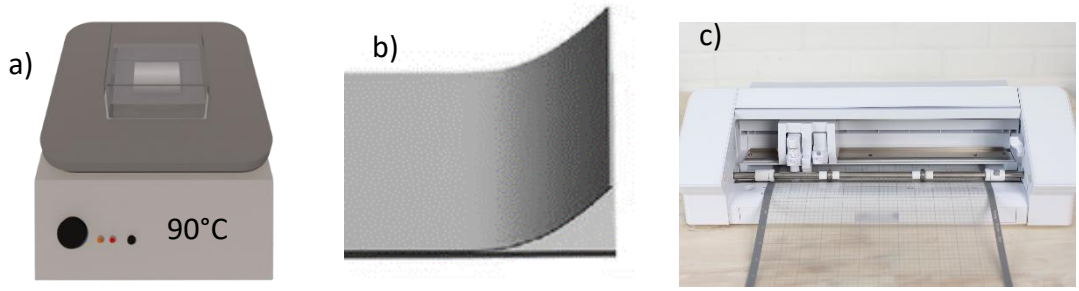

Figure 2.2 - a) removal of the glass substrate in a heated plaque at 90 ºC for a continuous period of time; b) laminating the metalized membranes onto the tattoo paper. c) cutting process on a silhouette cutter plotter of the desired circuit.

The produced temperature sensors were then characterized in a Polaron cryostat with a Keithley, in order to determine the resistance of the produced sensors (through IV curves analysis), as well as the variation of said resistance with a temperature change, to determine the TCR (temperature coefficient of resistance). The sensors were tested before Adhesion to the skin (before the transfer process, still on the paper). The produced sensors were also characterized in a 4 Point Probe FPP-50000, to determine their sheet resistance.

3

RESULTS AND DISCUSSION

3.1 Characterization of parylene and polyimide membranes

3.1.1 FTIR analysis

To detect the polar bonds, namely for the detection of organics, a FTIR analysis was performed. Organic materials usually exhibit multiple peaks due to the polar bonds between O-H, C-O and C-H. FTIR is then used to evaluate the chemical composition of the parylene and polyimide membranes and the results were compared with the basic materials (liquid polyimide and parylene dimers) and their commercial versions.

Figure 3.1 shows the ATR-FTIR spectra for the parylene membranes. In table 2 it is possible to identify notable bands of the parylene-C spectrum. The absence of a transmittance band in the region of ~1700 cm^{-1}, in the parylene dimer and parylene spectrums, indicate that here are no carbonyl or carboxylic bonds in the as-deposited film. [40]

Table 2 - Notable bands in the parylene films FTIR spectrum [41] .

Assignment	Wavenumber (cm−1)
Two neighboring H atoms bonded to aromatic ring vibrations	827
Cl bonded to aromatic ring vibrations	877; 1051
In-plane deformation of C-H bond in aromatic ring vibrations	1200; 1100
CH3 symmetric bending vibrations	1340
C-C deformation vibrations	1403
CH2 rocking vibrations	1452
C-C ring stretching vibrations	1495
Skeletal aromatic C-C vibrations	1557; 1607

The bands in the parylene membranes produced and the characteristic bands of the parylene in table 2 confirm the production of a parylene membrane. The diference of peaks between the dimer and the parylene membrane, spcifically in the 850 cm^{-1} to 700 cm^{-1} area are due to the polymerization of the parylene dimer.

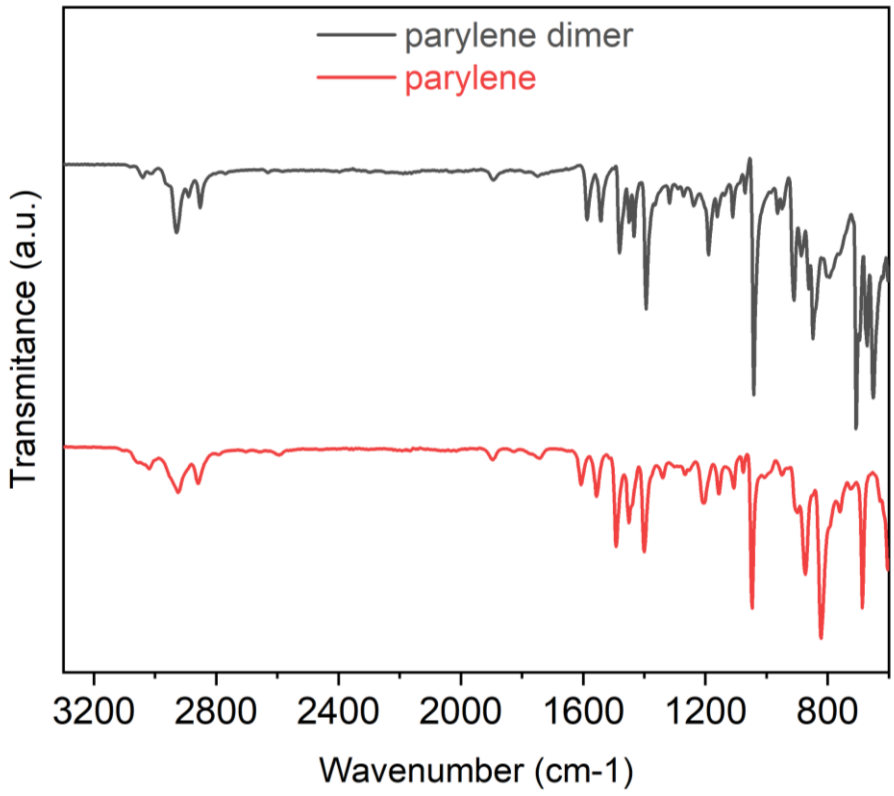

Figure 3.1 - ATR-FTIR spectrum of the parylene dimer and membranes.

In figure 3.2 is shown the ATR-FTIR spectrum of the polyimide membranes. The ATR-FTIR spectrum of polyimide membranes is characterized by main bands at around 1778 cm^{-1}, 1772 cm^{-1} (imide ring); 1498 cm^{-1} (phenylene); 1377 cm^{-1} (pyromellitic imide) and 1245 cm^{-1} (aromatic ether) [41], and the bands described in table 3. The band at 1 015 cm^{-1} that represents the vibration of the aromatic moieties was considered as an internal standard as it is invariant [42]. Due to the polyimide being a liquid, the spectrum presents some differences to the studied membranes. However, a comparison between the bands of the produced membrane and a commercial Kapton tape (same components), alongside the similarity of the samples to the characteristic bands of polyimide in a FTIR spectrum, allow the conclusion that the presented sample is a polyimide membrane.

Table 3 - Frequencies of characteristic bands of the polyimide FTIR spectrum [43].

Assignment	Wavenumber (cm^{-1})
C–C(=O)–C symmetric stretch (imide ring)	1780
C–C(=O)–C antisymmetric stretch (imide ring)	1720
Aromatic ring	1600; 1015
Aromatic CH	1500
Pyromellitic imide (CNC stretching)	1370
Aromatic C–O–C ether stretch	1270
(O=C–O or O=C–N)	888

;

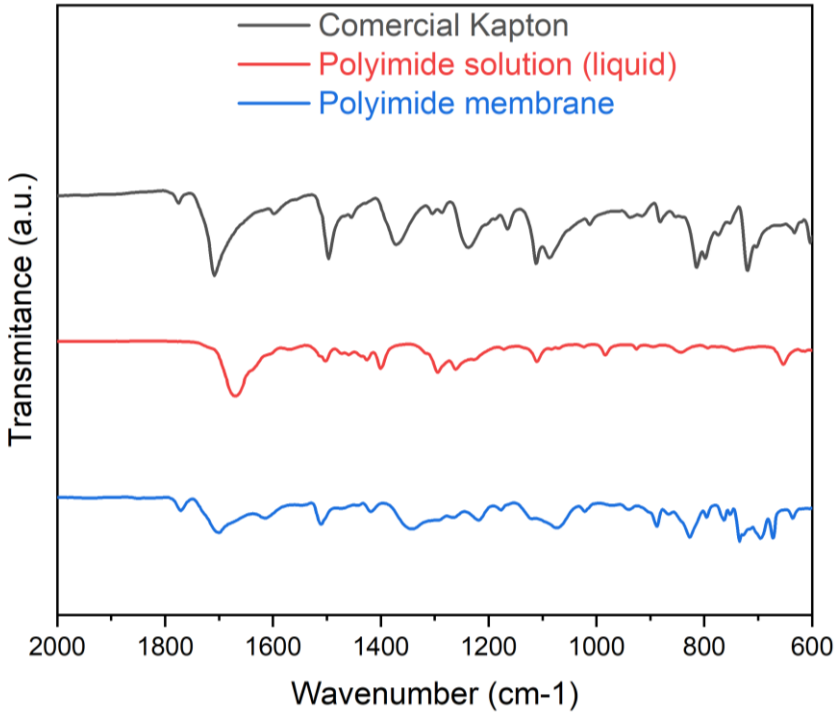

Figure 3.2 - ATR-FTIR spectrum of the polyimide membranes.

3.1.2 Differential Scanning Calorimetry analysis

The Differential Scanning Calorimetry (DSC) is one of the main techniques for thermal analysis. DSC detects endothermic and exothermic transitions like the determination of transformation temperatures and enthalpy of solids and liquids as a function of temperature. A DSC-TG analysis was performed in the produced parylene and polyimide membranes, a commercial polyimide membrane (Kapton) and to the tattoo paper. In figure 3.3, it's possible to view a DSC-TG curve, concerning mass loss, and DSC in function of temperature, for the tattoo paper. As is shown, the tattoo paper presents a slight peak at 66 ºC, and a slight mass change of -

5,55% at this temperature, which can be attributed to evaporation of water present in the sample. The peak at 330 ºC is attributed to the temperature of degradation of the tattoo paper, which also presents significant mass loss at such temperature in figure 3.3 b).

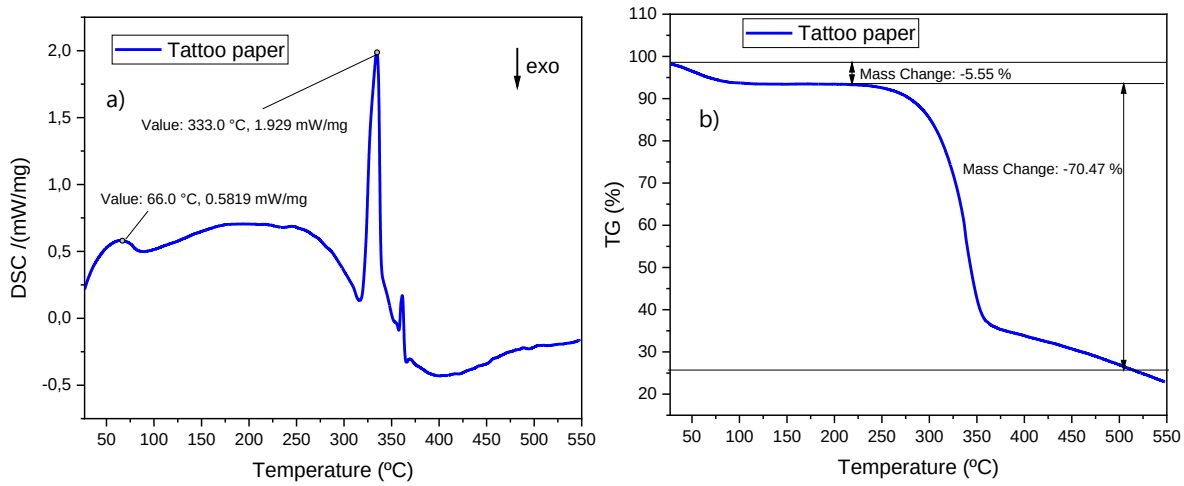

Figure 3.3 - DSC analysis of the tattoo paper; a) DSC peaks; b) Mass change during heating.

In figure 3.4 is depicted the DSC analysis of the parylene membranes, from 27 ºC (room temperature) to 550 ºC, at a rate of 5 °C/min.

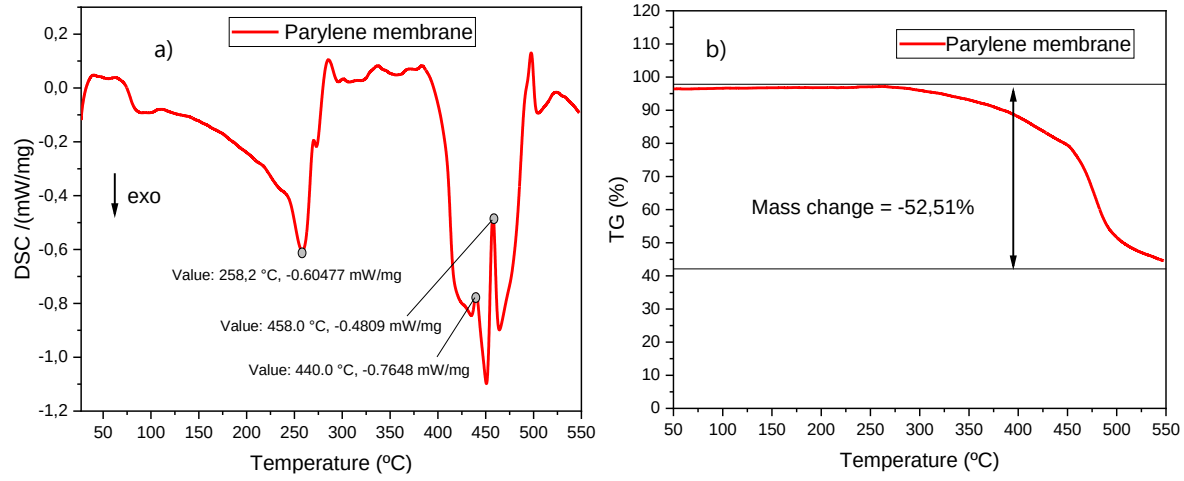

Figure 3.4 - DSC analysis of the parylene membranes; a) DSC peaks; b) Mass change during heating.

As its seen in figure 3.4a), the exothermic pic at 258.2 ºC can be attributed to a crystallinity rearrange in the parylene membrane, as it doesn't present any significant mass change in the sample. Although there are no mass changes at this temperature, crystallinity orientation changes can influence the mechanical resistance of the material, making it more fragile. Meanwhile, at 440 ºC and 458 ºC, the endothermic peaks, represents the temperature of degradation of the parylene membrane, as it coincides with a significant mass loss in figure 3.4 b).

Figure 3.5 shows the comparison between the DSC-TG curves and mass loss curves of the commercial Kapton membranes and the produced polyimide membranes. The similarity between both the curves indicates the presence of a polyimide film, that presents no significant mass loss, in both membranes, until 550 ºC. In figure 3.5a), the Kapton membrane presents a peak at 70 ºC, and in figure 3.5c) the polyimide membrane the slight peak is situated at 71 ºC, both with no significant mass loss. This indicates that at these temperatures, some internal rearrangements between the atoms that constitute the membranes occur, which can affect the stability of the membranes, but don't compromise the integrity of such. In figures 3.5 b) and d), is observed that, although the mass loss in the produced membranes is slightly higher at -5,16 %, compared to the -3,78 % of the Kapton membranes, these produced membranes maintain their integrity when submitted to high temperatures.

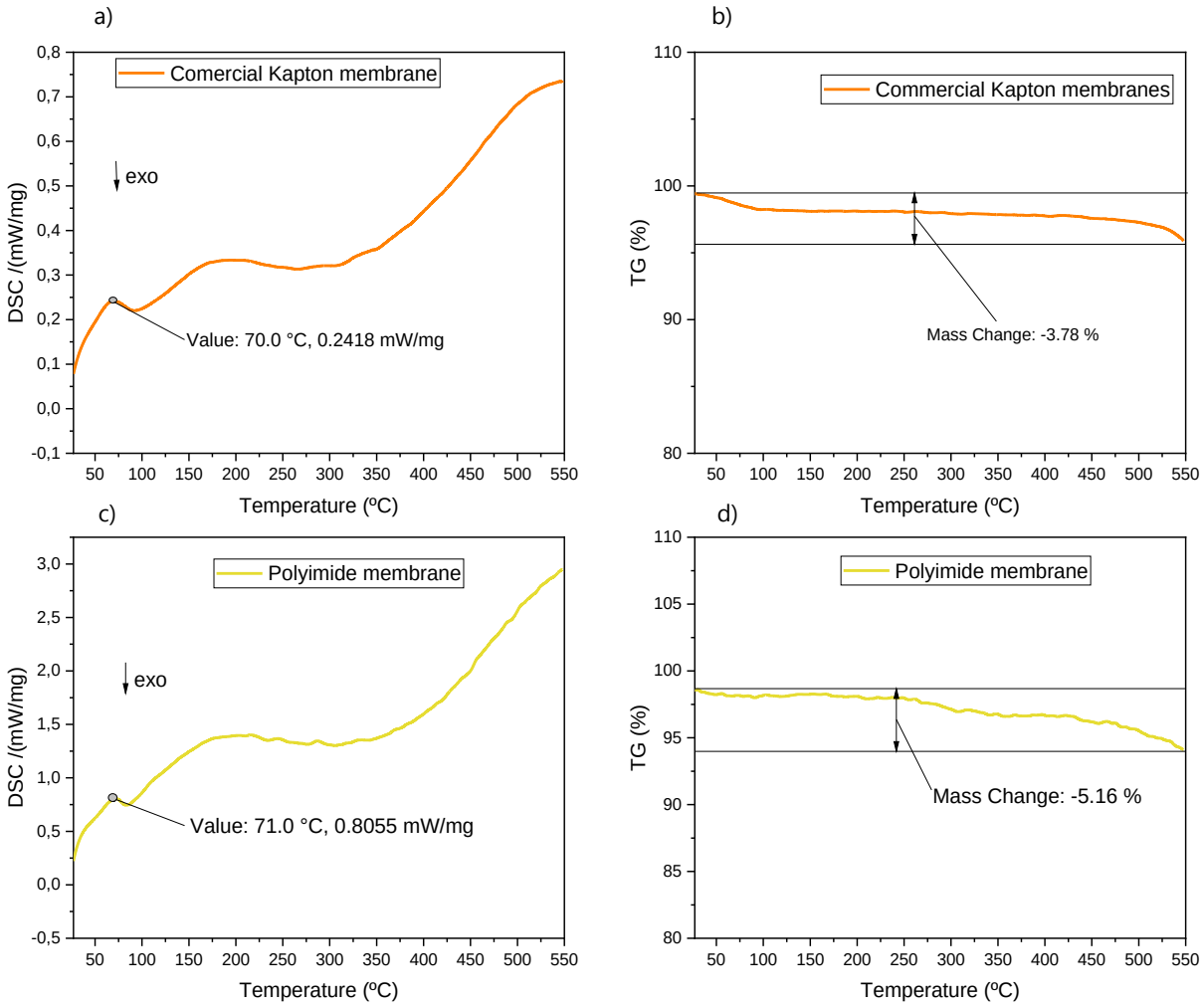

Figure 3.5 - DSC analysis of the commercial Kapton membranes; a) DSC peaks; b) Mass change during heating; and of the polyimide membranes: c) DSC peaks; d) Mass change during heating.

3.1.3 X-ray diffraction

X-ray diffraction is a technique often used to study the crystallographic structure of the samples under analysis. Moreover, this technique can also be used to detect the presence of different crystalline phases as well as quantify their weight fractions. This technique was used to evaluate the crystallographic structure of aluminum and gold films deposited onto parylene-C and polyimide substrates. The XRD diffractogram for the parylene membrane after peel-off, presented in figure 3.6, exhibits a peak at around 15 °, characteristic to parylene compounds [44], confirming the production a parylene membrane. The presence of a solo peak in parylene membranes attest to the semi-crystallinity of the polymer.

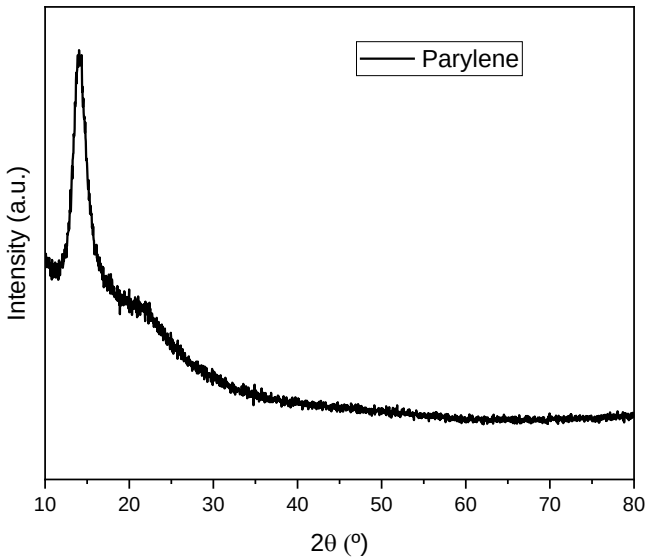

Figure 3.6 - XRD diffractogram of the parylene membranes.

An aluminum layer (100 nm) was deposited on top of the parylene-C membrane through thermal evaporation and the corresponding diffractogram is presented in figure 3.7. The characteristic peak of the parylene membranes is still present at 2θ=15º, and at around 38º and 45º are representative of the (111) and (200) planes, characteristic of the face-centered cubic (fcc) form of aluminum (ICDD card: 01-085-1327)[45]. Thus, the diffractogram of figure 3.7 indicates that the deposition of the aluminum layer does not interfere with the crystalline structure of the parylene-C membrane. The absence of peaks above 50 °, characteristic of the planes (220), (311) and (222) [46], is justified by the low thickness (100nm) of the aluminum layer present in the sample.

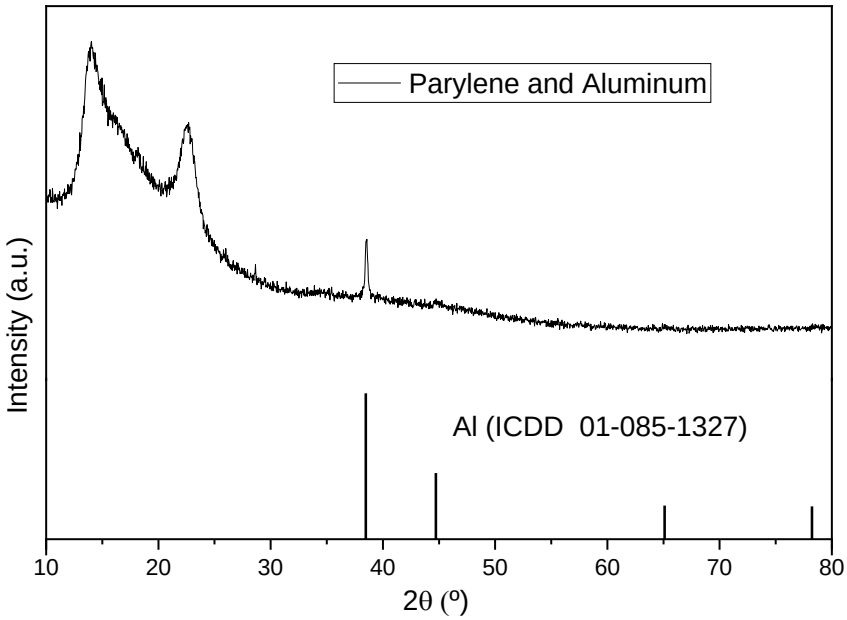

Figure 3.7 - XRD diffractogram of the parylene membranes with a 100 nm layer of aluminium.

Figure 3.8 depicts the diffractogram of parylene membranes after a deposition of a Ti/Au layer. Through the analysis of this figure, it is possible do detect the presence of the characteristic parylene peak at 2θ=15 º, although with a lower intensity. The remaining peaks coincide and present more compatibility with the characteristic peaks of gold compounds, namely at 2θ=38 º, 45 º, 65 º and 76 º. attributed to the (111), (200), (220) and (311) planes, respectively, which are characteristic of the structure of Au (ICDD card: 00-001-1172) [47] [48].

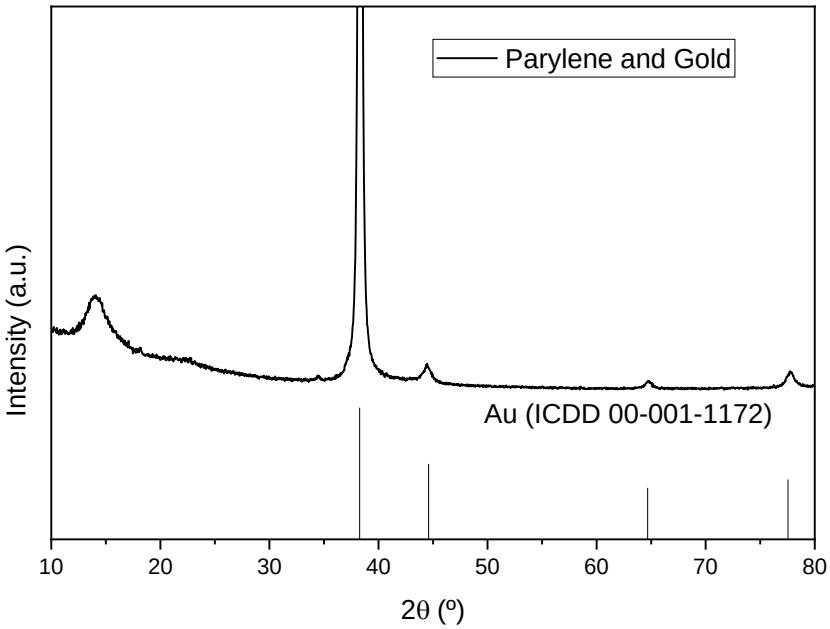

Figure 3.8 - XRD diffractogram of the parylene membranes with an 80 nm layer of gold.

In comparison, polyimide membranes with a 6 µm thickness were produced through spin-coating of a commercial polyimide solution (2611 from HD MicroSystems) onto a common glass substrate and their corresponding diffractogram, after peel-off is presented in figure 3.9. Only a slope at around 20 º can be detected in the polyimide membrane's diffractogram, which indicates that the produced polyimide membranes are amorphous [49].

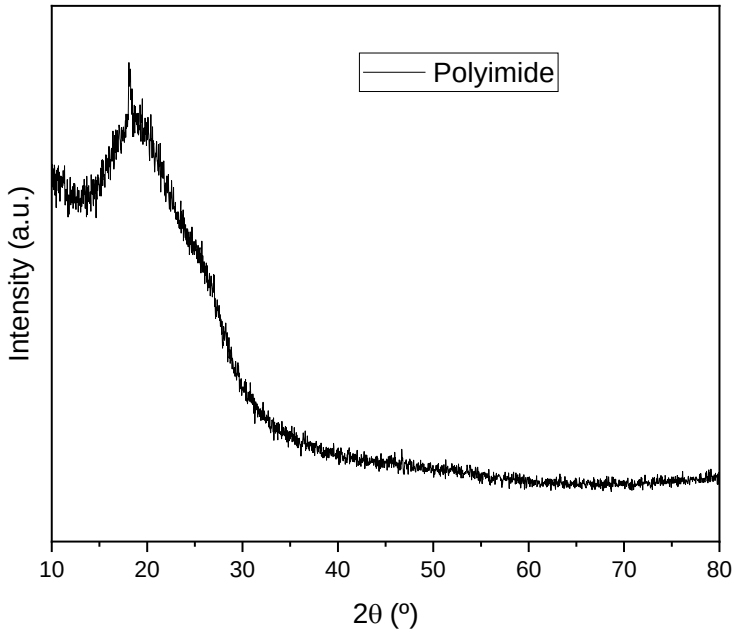

Figure 3.9 - XRD diffractogram of the polyimide membranes (6 µm).

Similarly, to the process performed for the parylene-C membranes a 100 nm aluminum layer and an 80 nm Au layer was deposited on top of the polyimide membranes. The corresponding diffractograms are presented in Figure 3.10 and Figure 3.11. The presence of a slight cluster at 20º, characteristic of the polyimide membrane, can be observed in figure 3.10. Additionally, the diffractogram presents peaks at 38 º and 45 º, similar to parylene membranes with aluminum, which are representative of the (111) and (200) planes, characteristic of the face-centered cubic (fcc) form of aluminum (ICDD card: 00-004-0787) [45], but, due to low thickness of the films (100nm), the peaks that usually characterize the aluminum above 60º are not presented, characteristic of the planes (220), (311) and (222) [46].

The diffractogram of the polyimide membrane covered with an 80 nm Au layer, is shown in figure 3.11. The characteristic slope of the amorphous polyimide membranes is still present at 2θ=20 º. The diffractogram peaks at 2θ=35 º, 38 º, 45 º and 65 º coincide with the (111), (200), (220) and (311) planes, characteristic of gold compounds (ICDD card: 00-001-1172) [47] [48], which supports the a presence of a gold layer on top of the polyimide sample.

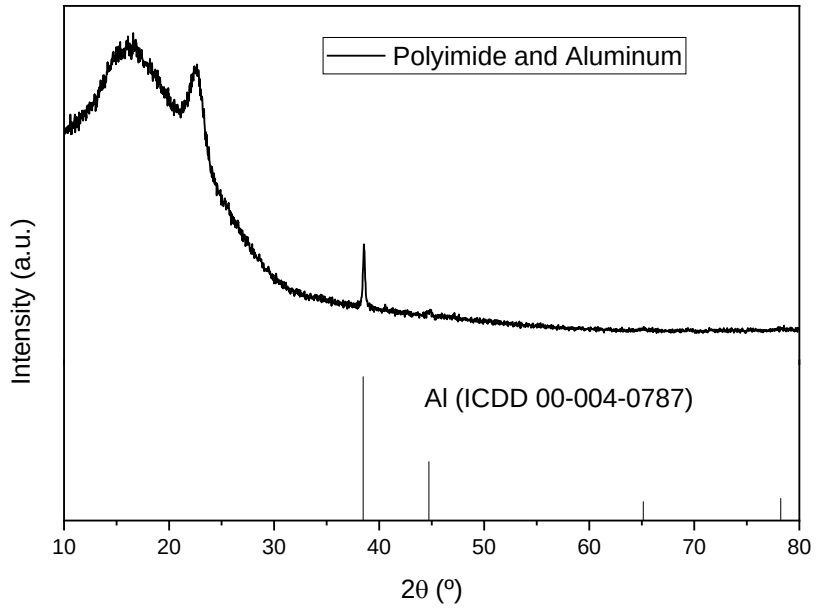

Figure 3.10 - XRD diffractogram of the polyimide membranes with a 100 nm layer of aluminium.

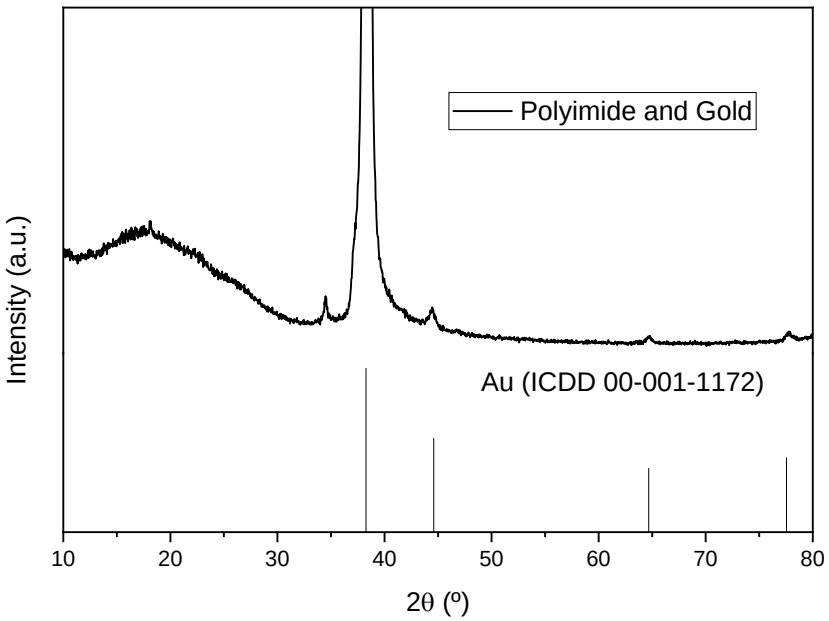

Figure 3.11 - XRD diffractogram of the parylene membranes with a 80 nm layer of gold.

3.2 Dimensioning and production of the e-tattoos

3.2.1 E-tattoo assembling

After the production of the polyimide membranes, they were metallized (with aluminum or gold), and the e-tattoos were produced, following the protocol previously showed, as is shown in figure 3.12.

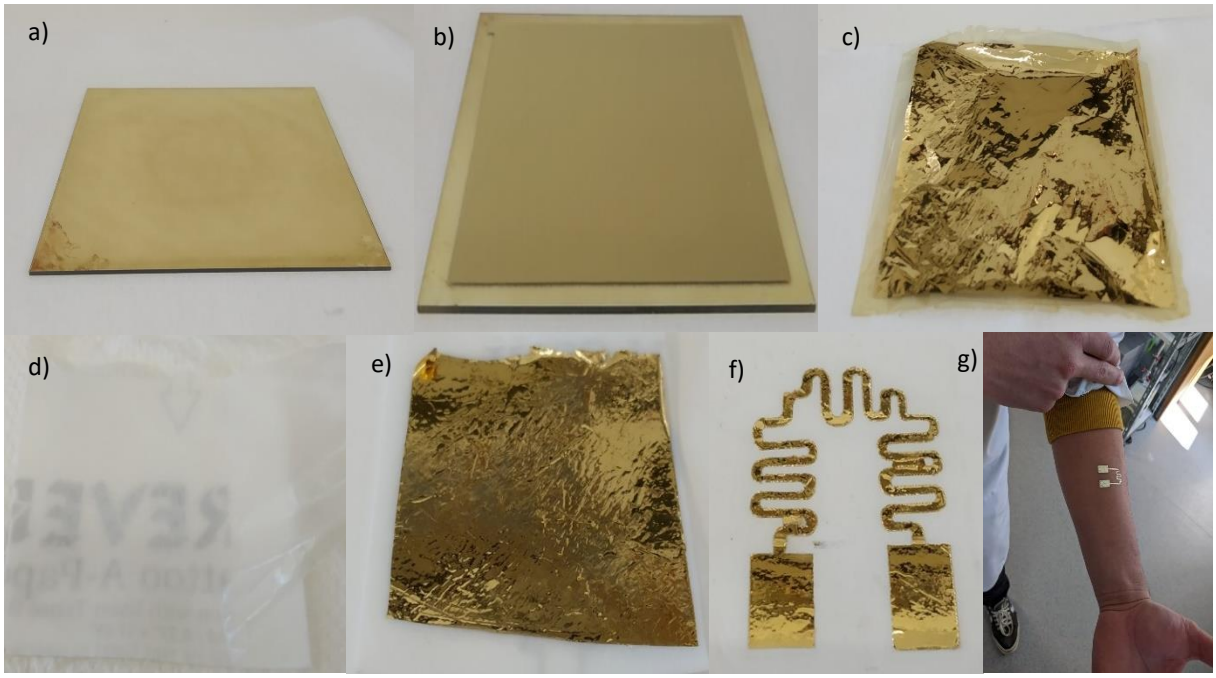

Figure 3.12 - E-tattoo assembling, full process: a) membrane production; b) metallization of the polymer membrane; c) peel-off of the metalized membrane; d) removal of the liner of the tattoo paper; e) sliding of the peeled-off membranes onto the tattoo paper; f) cutting of the circuit; g) application of the tattoo in the skin.

The final sensors were subdivided considering the constituting materials, polyimide and parylene, as well as if they are metalized with aluminum or gold. Additionally, the circuits were divided concerning the complexity of the serpentine circuit, a simpler and more complex design, illustrated in Annex III. The produced and tested sensors are depicted in figure 3.13 and table 4. It's important to refer, that the thicknesses presented here, are the programed deposited thickness of the metal films, in the thermal evaporator and e-beam thermal evaporator. The thickness of the membranes is the characteristic of the spin coating conditions, and curing temperature and time used in the fabrication process.

Table 4 - Overview of the design and constitution of the tested sensors.

Name	Membrane	Thickness	Metallization	Thickness	Design	Figure
Pl_Al A	Polyimide	6 µm	Aluminum	100 nm	Simple	3.13a)
Pl_Au A	Polyimide	6 µm	Ti/Au	86 nm	Simple	3.13b)
Par_Au	Parylene	6 µm	Ti/Au	86 nm	Simple	3.13c)
Pl_Au B	Polyimide	6 µm	Ti/Au	86 nm	Complex	3.14a)
Pl_Al B	Polyimide	6 µm	Aluminum	100 nm	Complex	3.14b)

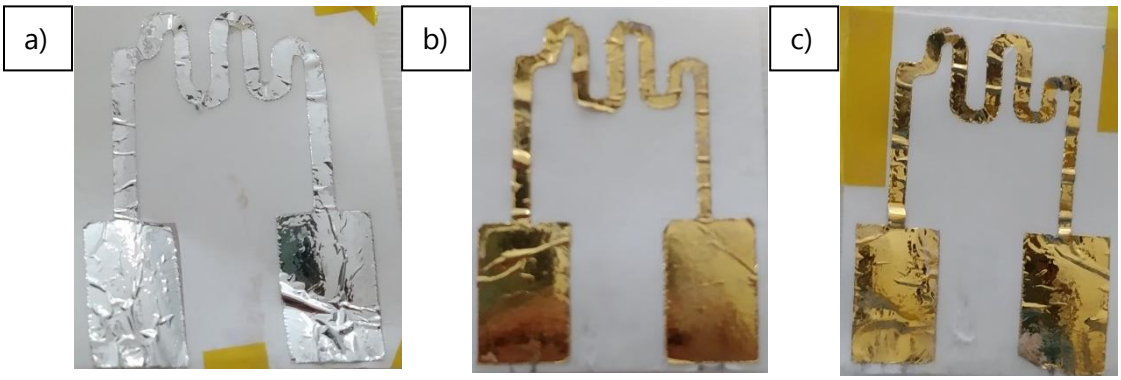

Figure 3.13 - Produced temperature sensing e-tattoos; a) Pl_Al A (polyimide and aluminium); b) Pl_Au A (polyimide and gold); Par_Au (parylene and gold).

Meanwhile, in figure 3.14a) and b) the more complex designs were prepared and were designated as Pl_Au B (polyimide with gold) and Pl_Al B (polyimide with aluminum), respectively.

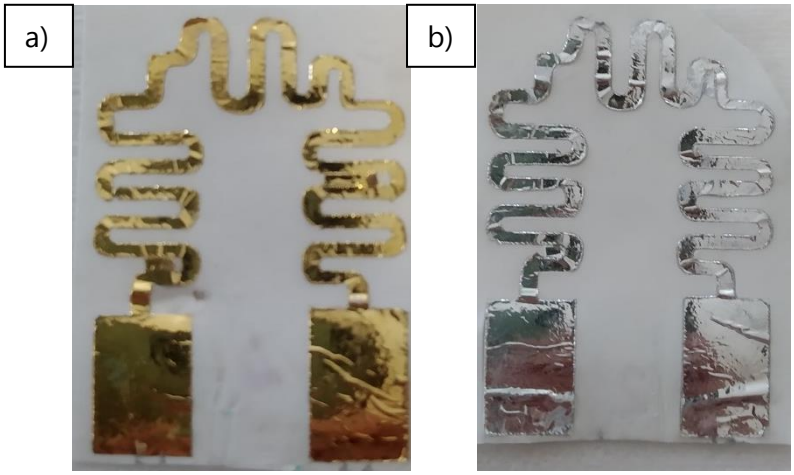

Figure 3.14 - Produced sensors for the more complex circuit design; a) Pl_Au B (polyimide and gold); b) Pl_Al B (polyimide and aluminium).

3.2.1 Sheet Resistance of the metalized membranes

The sheet resistance was determined through 4-Point probe analysis of the metalized membranes still on the glass substrate. This method consists in applying a current in the sample and viewing the tension response in the apparatus. The sheet resistance is then calculated through the following equation:

$$R_s = 4.532 \frac{V}{I} \quad (1)$$

Where I is the applied current, and V is the measured voltage.

In table 5, there are shown the voltage measurements from 1 mA through 5 mA applied current (with 1 mA increases) for the aluminum layers (in the polyimide and parylene).

Table 5 - Voltage measurements for aluminium layers.

Al on parylene		Al on polyimide	
Current (mA)	Voltage (mV)	Current (mA)	Voltage (mV)
1.00	0.17	1.00	0.25
2.00	0.33	2.00	0.50
3.00	0.49	3.00	0.74
4.00	0.65	4.00	0.98
5.00	0.81	5.00	1.22

Through equation 1, and due to the fact that the values of voltage increase linearly with the increase of the current, the average of sheet resistance for the aluminum layer on parylene is $0.74\ \Omega/\square$ and for the aluminum and polyimide sensors is $1.20\ \Omega/\square$. These values differ from the calculated value, accounting the resistivity and thickness of the material deposited (in Annex III), $0.28\ \Omega/\square$, possibly due to the non-uniformity of the deposited film, through thermal evaporation.

Similarly, in table 6, the same measurements are shown for the gold layers (also in the polyimide and parylene).

Table 6 - Voltage measurements for gold layers.

Au on parylene		Au on polyimide	
Current (mA)	Voltage (mV)	Current (mA)	Voltage (mV)
1.00	0.07	1.00	0.12
2.00	0.15	2.00	0.25
3.00	0.22	3.00	0.30
4.00	0.29	4.00	0.50
5.00	0.35	5.00	0.60

Through equation 1, and due to the fact that the values of voltage increase linearly with the increase of the current the value of sheet resistance for the gold on parylene layers is $0.32\ \Omega/\square$ and for the polyimide and gold sensors is $0.53\ \Omega/\square$.

These values are very similar to the calculated value (in Annex III), $0.31\ \Omega/\square$, which proves the stability of the polymer membranes metalized with gold, possibly due to gold being deposited though a different method (e-beam thermal evaporation), while comparing with aluminum.

3.3 Electrical characterization of the temperature sensors

3.3.1 Sensor´s nominal resistance

The resistance of the tested temperature sensors was determined by analysis of the IV curves, where a sample was clipped to a voltage source, and applied tension, between -0.5 V and 0.5 V, while the current (in mA) is measured. Through the analysis of the slope of the IV curve, it's possible to extract the value of the resistance of the sensor. The resistance value is extrapolated from a linear fit through the inverse of the slope.

The I-V curve for sensor PI_Al A is presented in figure 3.13a), and through analysis of the linear fit, the sensor possesses a Resistance of 1/slope that equals to 49.5 Ω.

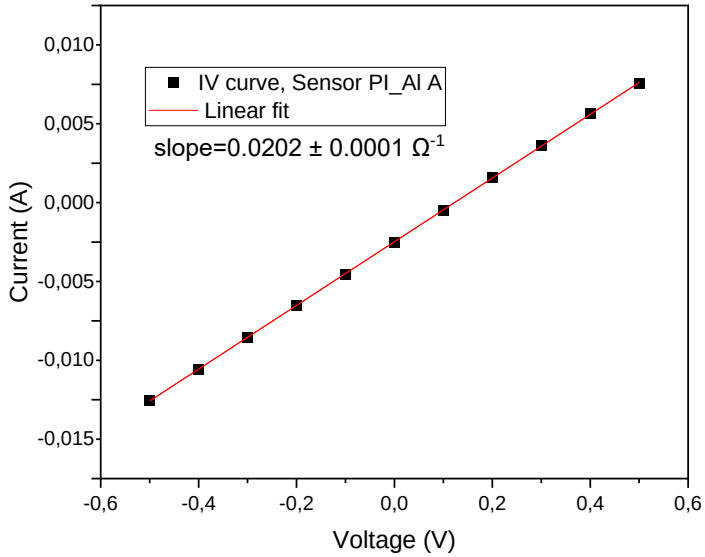

Figure 3.15 - Analysis of the IV curve for sensor PI_Al A.

In figure 3.16, Sensor PI_Au A, with polyimide with gold, with the same design as the previous sensor, is presented. Through the analysis of the slope in this sensor´s IV curve, the resistance value is 142.3 Ω, a value explained due to the continuous manipulation of the e-tattoos during the assembling process.

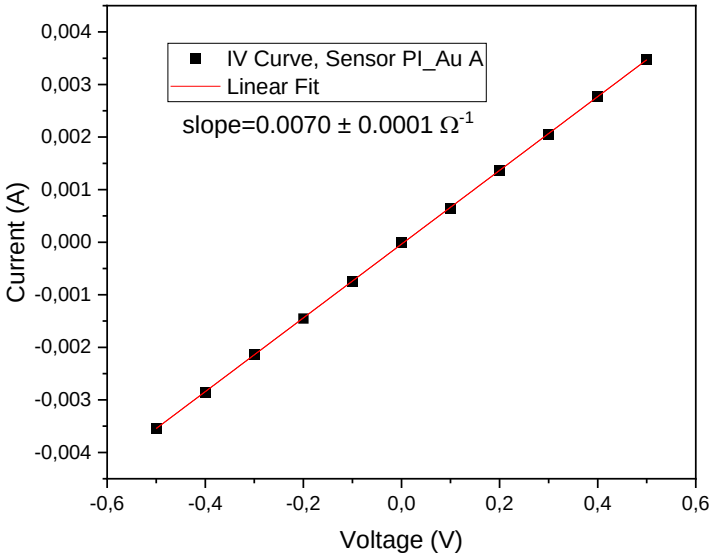

Figure 3.16 - Analysis of the IV curve for sensor PI_Au A.

In figure 3.17, the IV curve for the parylene and gold sensor, is presented. The design is the same as in figure 3.15 and 3.16, however, the resistance value for this sensor is 26.4 Ω, from the analysis of the IV curve, which represents a significant decrease comparatively to the previous sensor. This can be explained due to some constrains in the sensor, after the cutting process, as well as due to the lower adhesion of the gold to the parylene membrane.

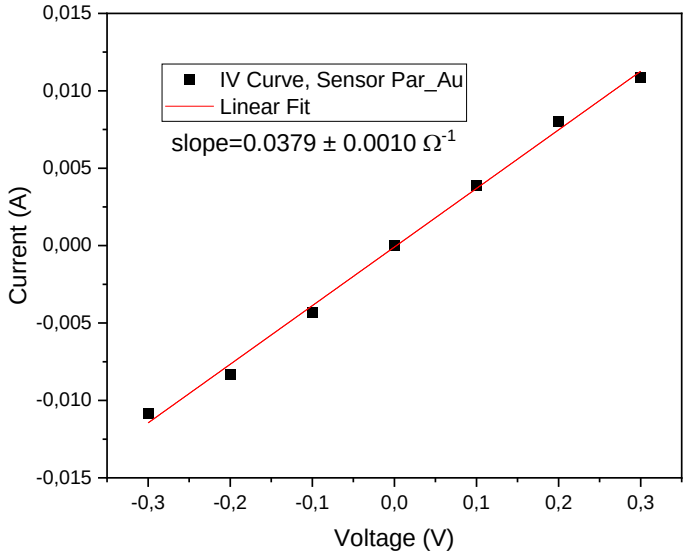

Figure 3.17 - Analysis of the IV curve for sensor Par_Au.

In figure 3.18, the IV curve for sensor PI_Au B, with the more complex design is shown. The resistance extrapolated from the IV curve for this sensor is 61.4 Ω. This value can be explained due to some constrains in the serpentines, that lead to less resistance. These constrains can be attributed to some irregularities in the cutting process or in the peeling-off of the extra remains after the cutting process. Finally, in figure 3.19, is depicted the IV curve for the polyimide and aluminum complex sensor (sensor PI_Al B). The value of resistance is 114.4 Ω from de IV slope. This sensor possesses a bigger resistance value than the simpler design of the circuit, however, has less resistance than the gold PI_Au A sensor.

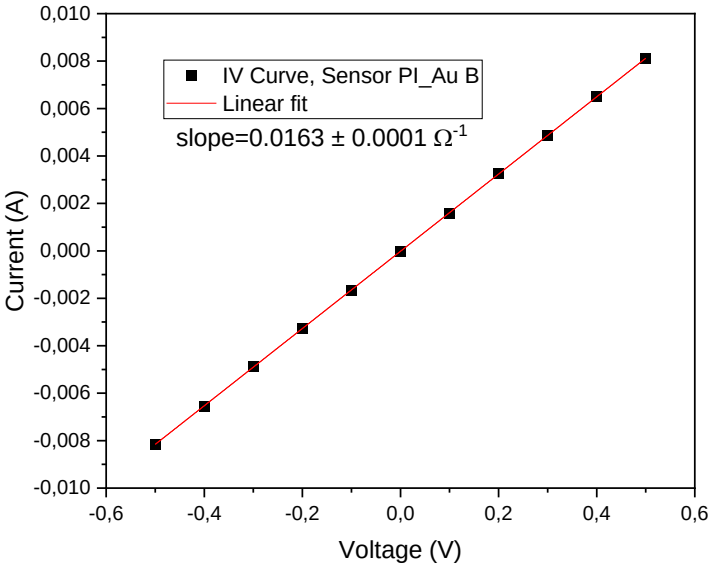

Figure 3.18 - Analysis of the IV curve for sensor PI_Au B.

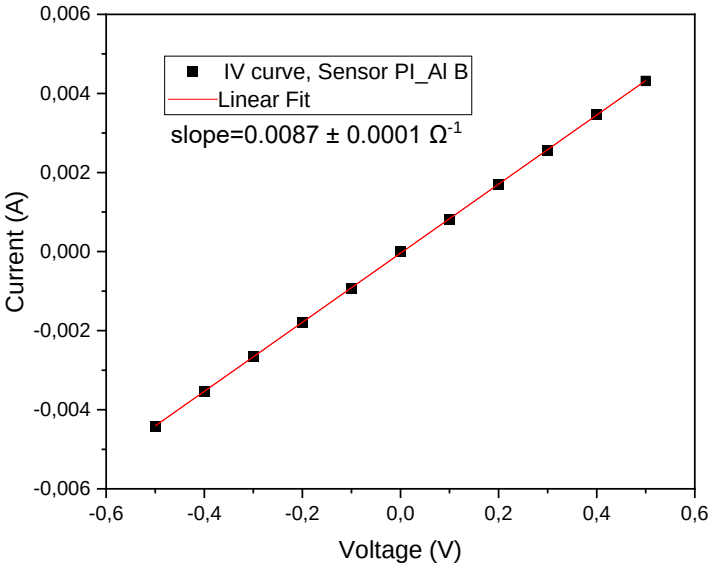

Figure 3.19 - Analysis of the IV curve for sensor PI_Al B.

3.3.2 TCR calculation for the temperature sensor

The TCR is a vital parameter for many practical applications of temperature sensor which refers to the relative change in resistance when the temperature changes. TCR can be calculated by equation 1.

$$R = R_0[1+\propto (T - T_0)](=) \propto = \frac{\left(\frac{\Delta R}{R_0}\right)}{T - T_0};\ TCR\ °C^{-1} \quad (2)$$

Where R_0 (Ω) represents the resistance value measured in the initial temperature T_0 (ºC) and ΔR is equal to $R - R_0$, and α is the TCR.

In table 7, are represented the values of TCR characteristics of aluminum and gold, the materials used in the produced sensors. The TCR analysis, consists in calculating the TCR of the different designed sensors and comparing them with the literature values [50].

Table 7 - TCR values for Aluminium and Gold [50];

Metal (bulk)	TCR ($ºC^{-1}$)
Al	0.0028
Au	0.0035

As shown in equation 1, the TCR can be calculated via the slope of a linear fit in a curve of the R/R_0 in function of T-T_0. Through these curves, the slope can directly correlate to the value of the temperature coefficient of resistance of the produced sensors. In the following analysis there are presented the graphs for the variation of R (resistance) in function of T (temperature)

as well as the graphs for the R/R_0 as a function of T-T_0, for the heating process, because the TCR values can be directly extrapolated from their slope.

In figure 3.20a), is shown the variation of the resistance with a temperature increase for sensor Pl_Al A. The TCR curve is shown in figure 3.20b), with the x values being T-T_0 and the y values being R/R_0, where R_0 value is 58.5 Ω for T_0=28.1 ºC. Through the analysis of a linear fit to the TCR graph, the extrapolated slope is representative of the TCR value for the first serpentine sensor, which is 0.0017 $ºC^{-1}$.

In figure 3.21a) the curve of resistance in function of temperature regards sensor Pl_Au A. Meanwhile in figure 3.21b), the TCR curve is presented for this sensor, with the R_0 value being 146.1 Ω for T_0=28.3 ºC. The slope of this linear fit, and TCR of sensor Pl_Au A is 0.0015 $ºC^{-1}$.

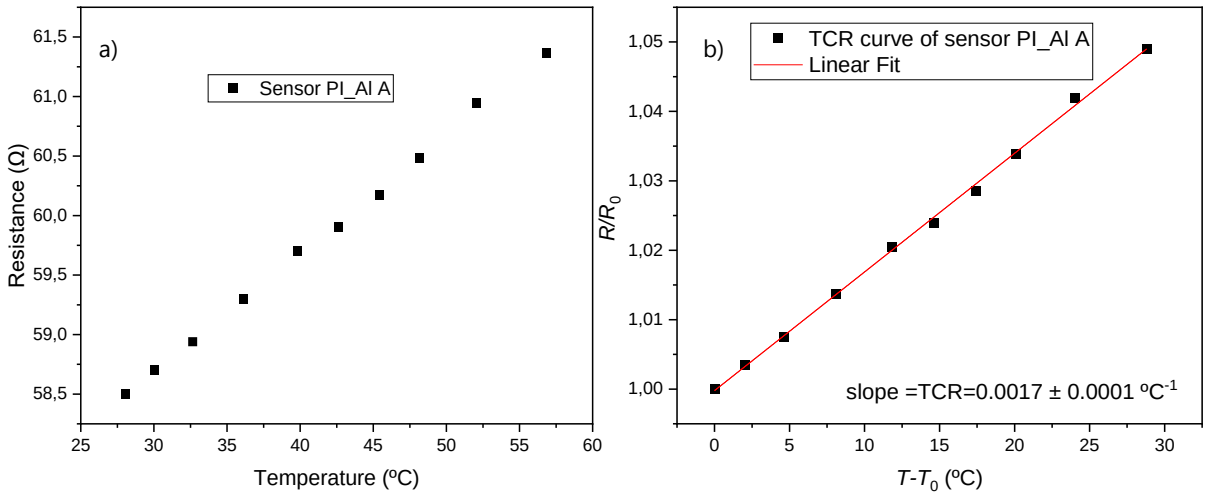

Figure 3.20 - Sensor Pl_Al A: a) Resistance variation with temperature increase; b) TCR curve.

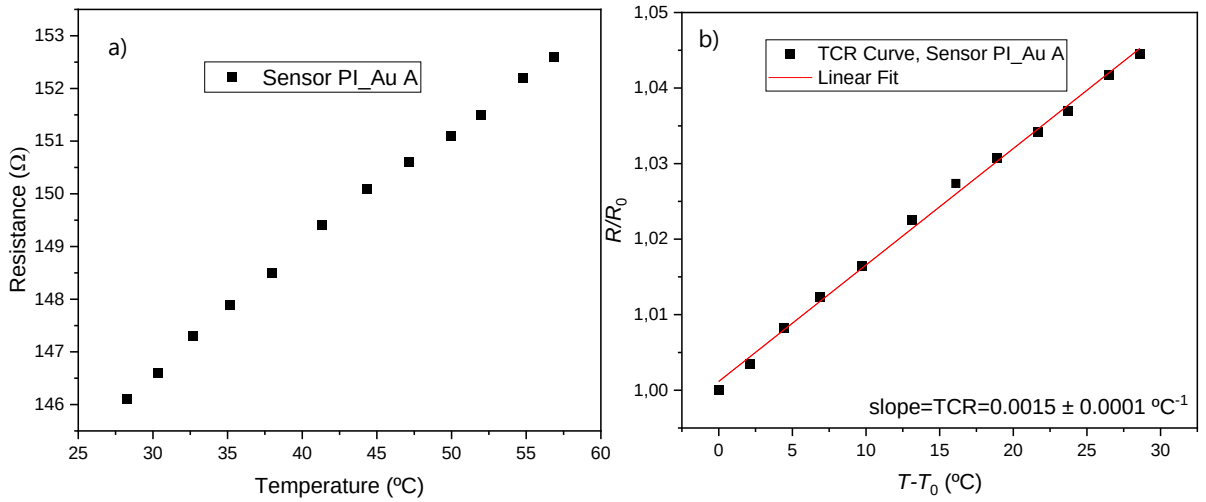

Figure 3.21 - Sensor Pl_Au A: a) Resistance variation with temperature increase; b) TCR curve.

The variation of resistance with temperature change for sensor Par_Au, is shown in figure 3.22a). The TCR curve, and respective linear fit, for this sensor is depicted in figure 3.22b), with a R_0 value of 22.0 Ω for T_0=28.4 ºC, the slope of this curve, and consequent TCR for this sensor is 0.0015 ºC^{-1}.

In figure 3.23a) the resistance variation with temperature is shown, for sensor PI_Au B, the more complexly designed gold sensor. The R_0 value for this sensor is 61.0 Ω at T_0=32.1 ºC, and through the analysis of the TCR curve, in figure 3.23b), the TCR value for sensor PI_Au B is 0.0017 ºC^{-1}.

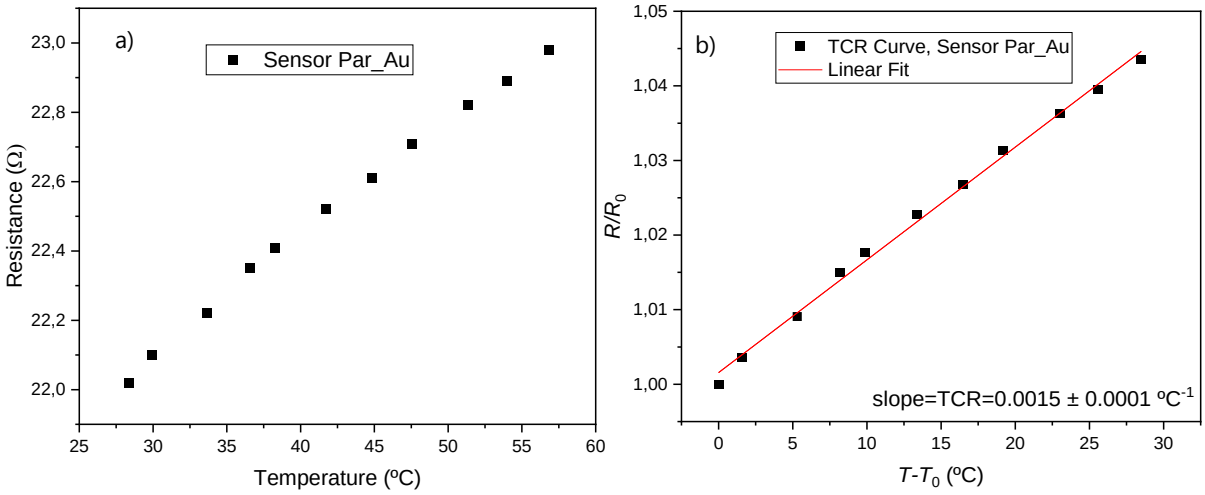

Figure 3.22 - Sensor Par_Au: a) Resistance variation with temperature increase; b) TCR curve.

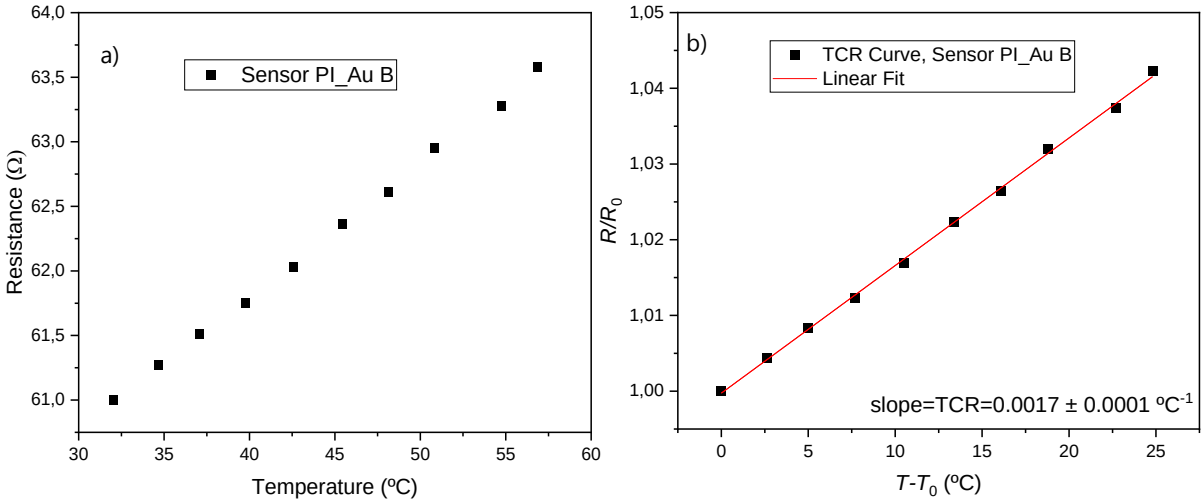

Figure 3.23 - Sensor PI_Au B: a) Resistance variation with temperature increase; b) TCR curve.

Finally, the study of sensor PI_Al B, englobes the variation of the resistance with temperature change, the TCR curve, during the heating process, and the TCR curve for the cooling process, in order to infer about the hysteresis and reproducibility of measurements. This sensor presents a R_0 of 116.3 Ω for T_0=28.3 ºC. In figure 3.24a) is shown the Resistance and temperature curve. Figure 3.24b) shows the TCR curve for the heating of the sensor, and figure 3.34c) depicts the TCR during cooling of the circuit. The value of this sensor´s TCR is the same, when in heating or in cooling mode, 0.0017 $ºC^{-1}$, which proves the absence of hysteresis of these sensors, as well as confirm the reproducibility of measurements, of these sensors. The TCR values for the cooling process, of the remaining sensors are discussed in Annex IV.

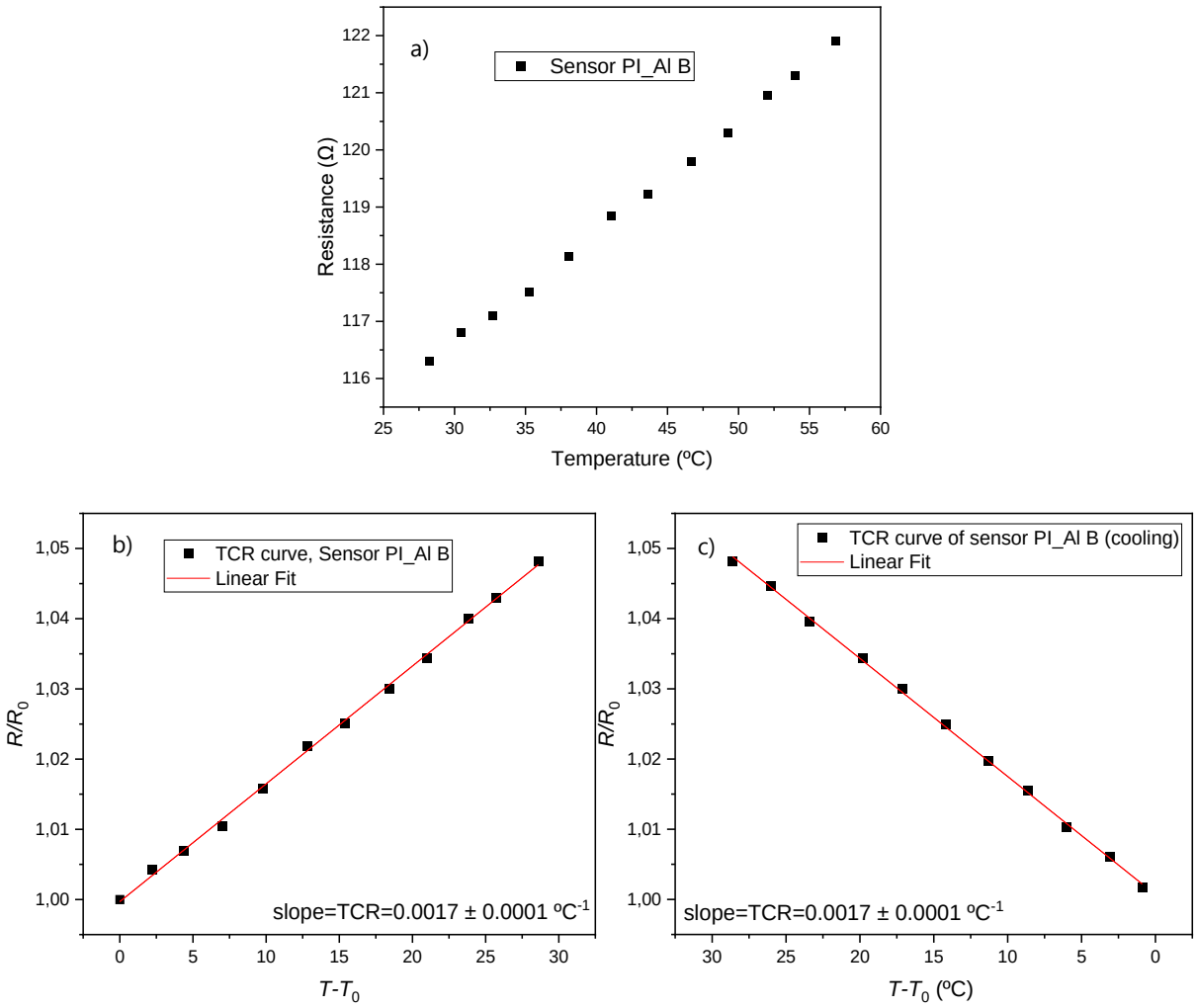

Figure 3.24 - Sensor PI_Al B: a) Resistance variation with temperature increase; b) TCR curve for the heating of the sample; c) TCR curve for the cooling of the sample.

The sensors present TCR values in the same decimal range as the theoretical value for aluminum, 0.0028 $°C^{-1}$ and for gold 0.0035 $°C^{-1}$, which means, that although they are lower values than the theoretical, the sensors still possess good temperature sensing capabilities. The difference between the obtained and theoretical values comes from the characteristic lower TCR for thin films in comparison to materials in bulk. [51]

In table 8, an overview is presented, of the sheet resistance, resistance, and TCR values obtained from the characterization of the produced sensors.

Table 8 - Overview of the obtained values of R_s, R and TCR for the tested sensors.

Sensor	R_s (Ω/□)	R (Ω)	TCR ($°C^{-1}$)
Pl_Al A	1.20	49.5	0.0017
Pl_Au A	0.53	142.3	0.0015
Par_Au	0.32	26.4	0.0015
Pl_Au B	0.53	61.4	0.0017
Pl_Al B	1.20	114.4	0.0017

4

Conclusion and future perspectives

The main objective of this work, which consisted in the development of e-tattoos using polymeric membranes prepared in CENIMAT, aiming the development of functional on-skin devices, was successfully achieved.

The use of polymeric membranes, prepared in our laboratory, has a huge advantage since the polymeric substrate supporting the functional device can be produced according to the desired needs and specifications such as thickness, mechanical and electric properties. The produced membranes, parylene and polyimide, presented a thickness of 6 µm, and also allowed the production of functional e-tattoos, that can be safely attached to the human skin due to their excellent mechanical stability.

As a case study, temperature sensors were developed based on this technology. The produced sensors, consisted in polyimide with an aluminum layer, presented a resistance value of 49.5 Ω for the simpler serpentine design and 114.4 Ω and for the more complex design. The value of TCR was 0.0017 $^{\circ}C^{-1}$ for both designs. Polyimide with gold temperature sensors were also produced, with resistance values of 61.4 Ω and 142.3 Ω and TCR values of 0.0015 $^{\circ}C^{-1}$ and 0.0017 $^{\circ}C^{-1}$ for the simpler and more complex design, respectively. Additionally, a parylene with gold sensor was also successfully produced, achieving a resistance value of 26.4 Ω and TCR of 0.0015 $^{\circ}C^{-1}$. With these values, it's possible to conclude, that the produced e-tattoos, are capable of functioning as temperature sensors.

In spite the progresses made in this work, there are still many milestones left to overcome, and based in the obtained results, there are some suggestions and future perspectives: experiment with surface treatments of the parylene membranes to improve the adhesion of the aluminum and gold to the substrate, which can improve the stability; develop other sensors to test the versatility, in the measurement of several other physiological features, such as electrocardiograms, humidity measurements or glucose monitoring.

5

BIBLIOGRAPHY

[1] A. J. Bandodkar, W. Jia, and J. Wang, "Tattoo-Based Wearable Electrochemical Devices: A Review," *Electroanalysis*, vol. 27, no. 3, pp. 562–572, 2015, doi: 10.1002/elan.201400537.

[2] D. H. Kim *et al.*, "Epidermal electronics," *Science (80-.).*, vol. 333, no. 6044, pp. 838–843, 2011, doi: 10.1126/science.1206157.

[3] J. Kim *et al.*, "Epidermal electronics with advanced capabilities in near-field communication," *Small*, vol. 11, no. 8, pp. 906–912, 2015, doi: 10.1002/smll.201402495.

[4] W. H. Yeo *et al.*, "Multifunctional epidermal electronics printed directly onto the skin," *Adv. Mater.*, vol. 25, no. 20, pp. 2773–2778, 2013, doi: 10.1002/adma.201204426.

[5] S. Wang *et al.*, "Mechanics of epidermal electronics," *J. Appl. Mech. Trans. ASME*, vol. 79, no. 3, pp. 1–7, 2012, doi: 10.1115/1.4005963.

[6] J. W. Jeong *et al.*, "Capacitive epidermal electronics for electrically safe, long-term electrophysiological measurements," *Adv. Healthc. Mater.*, vol. 3, no. 5, pp. 642–648, 2014, doi: 10.1002/adhm.201300334.

[7] M. Kaltenbrunner *et al.*, "An ultra-lightweight design for imperceptible plastic electronics," *Nature*, vol. 499, no. 7459, pp. 458–463, 2013, doi: 10.1038/nature12314.

[8] M. Melzer *et al.*, "Imperceptible magnetoelectronics," *Nat. Commun.*, vol. 6, pp. 1–8, 2015, doi: 10.1038/ncomms7080.

[9] J. R. Windmiller, A. J. Bandodkar, G. Valdés-Ramirez, S. Parkhomovsky, A. G. Martinez, and J. Wang, "Electrochemical sensing based on printable temporary transfer tattoos," *Chem. Commun.*, vol. 48, no. 54, pp. 6794–6796, 2012, doi: 10.1039/c2cc32839a.

[10] S. Kabiri Ameri *et al.*, "Graphene Electronic Tattoo Sensors," *ACS Nano*, vol. 11, no. 8, pp. 7634–7641, 2017, doi: 10.1021/acsnano.7b02182.

[11] R. C. Qian and Y. T. Long, "Wearable Chemosensors: A Review of Recent Progress," *ChemistryOpen*, vol. 7, no. 2, pp. 118–130, 2018, doi: 10.1002/open.201700159.

[12] T. Ha *et al.*, "A Chest-Laminated Ultrathin and Stretchable E-Tattoo for the Measurement of Electrocardiogram, Seismocardiogram, and Cardiac Time Intervals," *Adv. Sci.*, vol. 6, no. 14, 2019, doi: 10.1002/advs.201900290.

[13] H. Jeong *et al.*, "Modular and Reconfigurable Wireless E-Tattoos for Personalized Sensing," *Adv. Mater. Technol.*, vol. 4, no. 8, pp. 1–13, 2019, doi:

10.1002/admt.201900117.

[14] H. H. Asada, P. Shaltis, A. Reisner, S. Rhee, and R. C. Hutchinson, "Mobile Monitoring with Wearable Photoplethysmographic Biosensors," *IEEE Eng. Med. Biol. Mag.*, vol. 22, no. 3, pp. 28–40, 2003, doi: 10.1109/MEMB.2003.1213624.

[15] H. Bin Yao *et al.*, "A flexible and highly pressure-sensitive graphene-polyurethane sponge based on fractured microstructure design," *Adv. Mater.*, vol. 25, no. 46, pp. 6692–6698, 2013, doi: 10.1002/adma.201303041.

[16] B. Nie, R. Li, J. D. Brandt, and T. Pan, "Iontronic microdroplet array for flexible ultrasensitive tactile sensing," *Lab Chip*, vol. 14, no. 6, pp. 1107–1116, 2014, doi: 10.1039/c3lc50994j.

[17] A. Sezer Hicyilmaz and A. Celik Bedeloglu, "Applications of polyimide coatings: a review," *SN Appl. Sci.*, vol. 3, no. 3, pp. 1–22, 2021, doi: 10.1007/s42452-021-04362-5.

[18] I. Gouzman, E. Grossman, R. Verker, N. Atar, A. Bolker, and N. Eliaz, "Advances in Polyimide-Based Materials for Space Applications," *Adv. Mater.*, vol. 31, no. 18, pp. 1–15, 2019, doi: 10.1002/adma.201807738.

[19] H. Gao, X. Lan, L. Liu, X. Xiao, Y. Liu, and J. Leng, "Study on performances of colorless and transparent shape memory polyimide film in space thermal cycling, atomic oxygen and ultraviolet irradiation environments," *Smart Mater. Struct.*, vol. 26, no. 9, 2017, doi: 10.1088/1361-665X/aa7bd7.

[20] Y. S. Hsiao, W. T. Whang, S. C. Wu, and K. R. Chuang, "Chemical formation of palladium-free surface-nickelized polyimide film for flexible electronics," *Thin Solid Films*, vol. 516, no. 12, pp. 4258–4266, 2008, doi: 10.1016/j.tsf.2007.12.166.

[21] K. S. Karim and S. Abbaszadeh, "Radiation detector system and method of manufacture," vol. 2, no. 12, 2016.

[22] T. Xiao, X. Fan, D. Fan, and Q. Li, "High thermal conductivity and low absorptivity/ emissivity properties of transparent fluorinated polyimide films," *Polym. Bull.*, vol. 74, no. 11, pp. 4561–4575, 2017, doi: 10.1007/s00289-017-1974-6.

[23] K. Y. Huang, Y. S. Jhuo, P. S. Wu, C. H. Lin, Y. H. Yu, and J. M. Yeh, "Electrochemical studies for the electroactivity of amine-capped aniline trimer on the anticorrosion effect of as-prepared polyimide coatings," *Eur. Polym. J.*, vol. 45, no. 2, pp. 485–493, 2009, doi: 10.1016/j.eurpolymj.2008.10.033.

[24] S. A. Jenekhe, "The rheology and spin coating of polyimide solutions," *Polym. Eng. Sci.*, vol. 23, no. 15, pp. 830–834, 1983, doi: 10.1002/pen.760231508.

[25] H. W. Jeong, K. Kim, and H. Park, "(12) United States Patent," vol. 2, 2020.

[26] J. Boudaden *et al.*, "Polyimide-based capacitive humidity sensor," *Sensors (Switzerland)*, vol. 18, no. 5, pp. 1–15, 2018, doi: 10.3390/s18051516.

[27] J. A. Dobrzynska and M. A. M. Gijs, "Flexible polyimide-based force sensor," *Sensors*

Actuators, A Phys., vol. 173, no. 1, pp. 127–135, 2012, doi: 10.1016/j.sna.2011.11.006.

[28] T. Haggren *et al.*, "Nanowire encapsulation with polymer for electrical isolation and enhanced optical properties," *Nano Res.*, vol. 10, no. 8, pp. 2657–2666, 2017, doi: 10.1007/s12274-017-1468-8.

[29] M. Golda-Cepa, K. Engvall, M. Hakkarainen, and A. Kotarba, "Recent progress on parylene C polymer for biomedical applications: A review," *Prog. Org. Coatings*, vol. 140, no. October 2019, p. 105493, 2020, doi: 10.1016/j.porgcoat.2019.105493.

[30] P. H. Sonksen *et al.*, "[4] "Circadian variations of blood sugar and plasma insulin levels in man "Diurnal patterns of blood glu- cose, serum free fatty acids, insulin, glucagon and growth hormone in normal and juvenile diabetics Parylene as a Chronically Stable, Reproducible Mi," *J. Clin. Invest. Med. Diabetes Invest. Diabetol. Diabetol.*, vol. 463, no. 7, pp. 1954–1967, 1977.

[31] M. Lin *et al.*, "Flexible polymer device based on parylene-C with memory and temperature sensing functionalities," *Polymers (Basel).*, vol. 9, no. 8, pp. 1–9, 2017, doi: 10.3390/polym9080310.

[32] D. Huang, H. Wang, J. Li, Y. Chen, and Z. Li, "A WIRELESS FLEXIBLE WEARABLE BIOPOTENTIAL ACQUISITION SYSTEM UTILIZING PARYLENE BASED MICRONEEDLE ARRAY National Key Laboratory of Nano / Micro Fabrication Technology , Institute of Micro / Nano School of Information and Communication Engineering , Univer," *2019 20th Int. Conf. Solid-State Sensors, Actuators Microsystems Eurosensors XXXIII (TRANSDUCERS EUROSENSORS XXXIII)*, no. June, pp. 298–301, 2019.

[33] Y. Su *et al.*, "Printable, Highly Sensitive Flexible Temperature Sensors for Human Body Temperature Monitoring: A Review," *Nanoscale Res. Lett.*, vol. 15, no. 1, 2020, doi: 10.1186/s11671-020-03428-4.

[34] S. Y. Hong *et al.*, "Stretchable Active Matrix Temperature Sensor Array of Polyaniline Nanofibers for Electronic Skin," *Adv. Mater.*, vol. 28, no. 5, pp. 930–935, 2016, doi: 10.1002/adma.201504659.

[35] A. Chortos, J. Liu, and Z. Bao, "Pursuing prosthetic electronic skin," *Nat. Mater.*, vol. 15, no. 9, pp. 937–950, 2016, doi: 10.1038/nmat4671.

[36] T. Q. Trung, S. Ramasundaram, B. U. Hwang, and N. E. Lee, "An All-Elastomeric Transparent and Stretchable Temperature Sensor for Body-Attachable Wearable Electronics," *Adv. Mater.*, vol. 28, no. 3, pp. 502–509, 2016, doi: 10.1002/adma.201504441.

[37] R. C. Webb *et al.*, "Ultrathin conformal devices for precise and continuous thermal characterization of human skin," *Nat. Mater.*, vol. 12, no. 10, pp. 938–944, 2013, doi: 10.1038/nmat3755.

[38] Z. Liu *et al.*, "A thin-film temperature sensor based on a flexible electrode and substrate," *Microsystems Nanoeng.*, vol. 7, no. 1, 2021, doi: 10.1038/s41378-021-00271-0.

[39] E. Meng, P. Y. Li, and Y. C. Tai, "A biocompatible Parylene thermal flow sensing array,"

Sensors Actuators, A Phys., vol. 144, no. 1, pp. 18–28, 2008, doi: 10.1016/j.sna.2007.12.010.

[40] M. J. Herman and M. W. Blair, "Determination of chemical decay mechanisms of Parylene-C during X-ray irradiation using two-dimensional correlation FTIR," *Polym. Degrad. Stab.*, vol. 171, p. 109024, 2020, doi: 10.1016/j.polymdegradstab.2019.109024.

[41] T. Goda, T. Konno, M. Takai, and K. Ishihara, "Photoinduced phospholipid polymer grafting on Parylene film: Advanced lubrication and antibiofouling properties," *Colloids Surfaces B Biointerfaces*, vol. 54, no. 1, pp. 67–73, 2007, doi: 10.1016/j.colsurfb.2006.09.006.

[42] K. P. Pramoda, T. S. Chung, S. L. Liu, H. Oikawa, and A. Yamaguchi, "Characterization and thermal degradation of polyimide and polyamide liquid crystalline polymers," *Polym. Degrad. Stab.*, vol. 67, no. 2, pp. 365–374, 2000, doi: 10.1016/S0141-3910(99)00138-X.

[43] K. P. Pramoda, S. Liu, and T. S. Chung, "Thermal imidization of the precursor of a liquid crystalline polyimide," *Macromol. Mater. Eng.*, vol. 287, no. 12, pp. 931–937, 2002, doi: 10.1002/mame.200290027.

[44] M. A. Surmeneva *et al.*, "Effect of parylene C coating on the antibiocorrosive and mechanical properties of different magnesium alloys," *Appl. Surf. Sci.*, vol. 427, pp. 617–627, 2018, doi: 10.1016/j.apsusc.2017.08.066.

[45] N. Arora and B. R. Jagirdar, "Monodispersity and stability: Case of ultrafine aluminium nanoparticles (<5 nm) synthesized by the solvated metal atom dispersion approach," *J. Mater. Chem.*, vol. 22, no. 18, pp. 9058–9063, 2012, doi: 10.1039/c2jm16764f.

[46] S. R. Ghanta and K. Muralidharan, "Chemical synthesis of aluminum nanoparticles," *J. Nanoparticle Res.*, vol. 15, no. 6, pp. 1–10, 2013, doi: 10.1007/s11051-013-1715-1.

[47] A. F. Lee *et al.*, "Structural and catalytic properties of novel Au/Pd bimetallic colloid particles. EXAFS, XRD, and acetylene coupling," *J. Phys. Chem.*, vol. 99, no. 16, pp. 6096–6102, 1995, doi: 10.1021/j100016a053.

[48] A. N. Geraldes *et al.*, "Ethanol electro-oxidation in an alkaline medium using Pd/C, Au/C and PdAu/C electrocatalysts prepared by electron beam irradiation," *Electrochim. Acta*, vol. 111, pp. 455–465, 2013, doi: 10.1016/j.electacta.2013.08.021.

[49] T. Sawada and S. Ando, "Synthesis, Characterization, and Optical Properties of Metal-Containing Fluorinated Polyimide Films," *Chem. Mater.*, vol. 10, no. 11, pp. 3368–3378, 1998, doi: 10.1021/cm980051j.

[50] R. B. Belser and W. H. Hicklin, "Temperature coefficients of resistance of metallic films in the temperature range 25°to 600°C," *J. Appl. Phys.*, vol. 30, no. 3, pp. 313–322, 1959, doi: 10.1063/1.1735158.

[51] J. Rölke, "Nichrome Thin Film Technology and Its Application," *Electrocompon. Sci. Technol.*, vol. 9, no. 1, pp. 51–57, 1981, doi: 10.1155/APEC.9.51.

6

ANNEXES

Annex I. Surface treatment of the membranes

In figure x, is shown the result (on the right) of a surface treatment of the polyimide membrane before thermal evaporation. A dry etching was performed in sample at 50mT pressure and 10.0 sccm of O_2 during 200 seconds. Figure 6.1a) represents a polyimide membrane with evaporated aluminum, without any surface treatment. Meanwhile, figure 6.2b) represents a polyimide sample dry etched before thermal evaporation. As it can be seen, the sample after dry etching presents a burnt non-conductive layer of aluminum, which leads to the uselessness of the sample. Although initially it was thought to be a good process to improve the stability of the membranes and improve the adhesion of the metals to the membrane, this process doesn't work in polyimide membranes

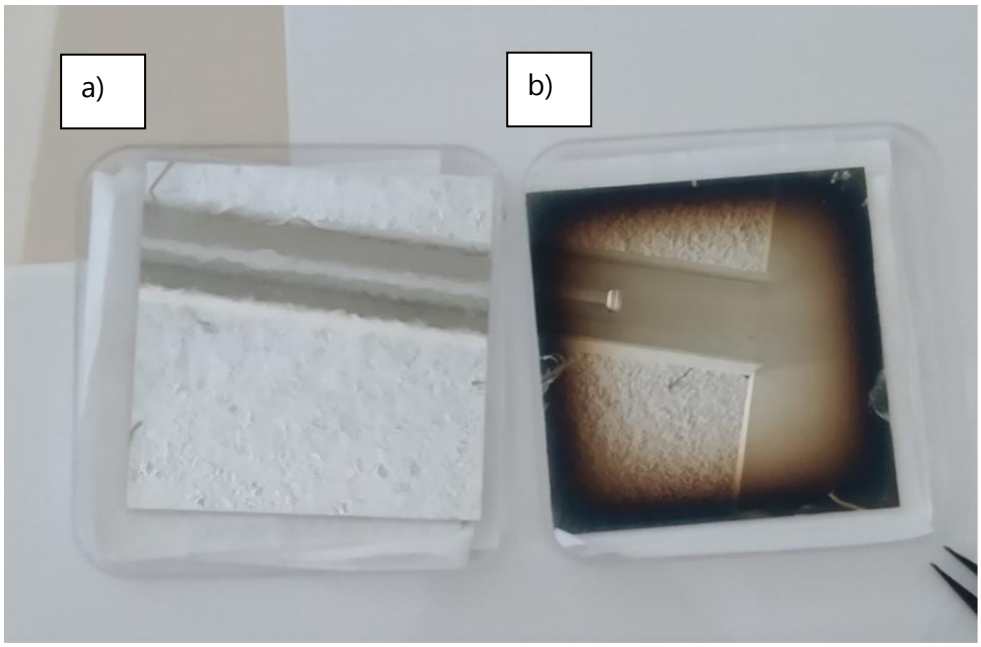

Figure 6.1 - Membranes after thermal evaporation: a) without dry etching treatment; b) with dry etching surface treatment.

Annex II. Cutting trials

In table 5, it is shown the cutting trials of the Silhouette Cameo 4 cutter plotter, for a layer of 6µm of polyimide (PI) and 100 nm Al and 6µm of polyimide (PI) + 86 nm of Ti/Au (the same force and blade were used for the Al and to the Au). The cutter plotter must have the necessary force, velocity, blade, and number of passings in order to only cut the membrane, maintaining the integrity of the tattoo paper. The force and blade are the main parameters to change, as they are the ones who most influence the cutting depth. The thinner the membrane to cut, the lower the force and smaller the blade to use. The velocity and number of passings stayed the same for all the samples, of parylene and polyimide.

Table 9 - Cutting trials for the polyimide and Al, and Ti/Au membranes.

Blade	Force	Results
1	1	No cut
1	2	No cut
1	3	Can cut
1	4	Can cut
1	5	Starts cutting the paper
2	1	No cut
2	2	Can cut
2	3	Can cut
2	4	Optimal cut
2	5	Starts cutting the paper

Additionally, in table 6, it is possible to observe the cutting trials for the parylene membrane (6 µm with 86 nm of Ti/Au and with 100 nm of Al). The results were similar to the polyimide membranes, however, as was previously mentioned, the cutting process of the parylene membranes was easier, so it required less force to cut the desired circuit.

It is important to refer, that due to the polyimide and parylene membranes being responsible for the main thickness of the final sensor (6µm), the cutting process with aluminum and gold presents the same optimal cutting specifications. Additionally, with such thin film membranes, the cutting processes didn't exceed the 5 force which began with consequent destruction of the sample.

Table 10 - Cutting trials for the parylene and Al, and Ti/Au membranes.

Blade	Force	Results
1	1	No cut
1	2	Can cut slightly
1	3	Can cut
1	4	Optimal cut
1	5	Starts cutting the paper
2	1	Can cut slightly
2	2	Can cut
2	3	Can cut
2	4	Stars cutting the paper

Annex III. Determination of the theoretical resistance of the sensors

The determination of the resistance of the sensors starts with subdividing the sensor design in pads and squares of 0.2 mm width.

The first designed sensor, in figure 6a) and the more complex design is depicted in figure 6b); The first sensor, with the simpler circuit presented about 200 squares, with 16 corner squares and the 2 big pads at the bottom. The more complex sensor consists of approximately 500 squares, 50 corner squares and 2 big pads as well.

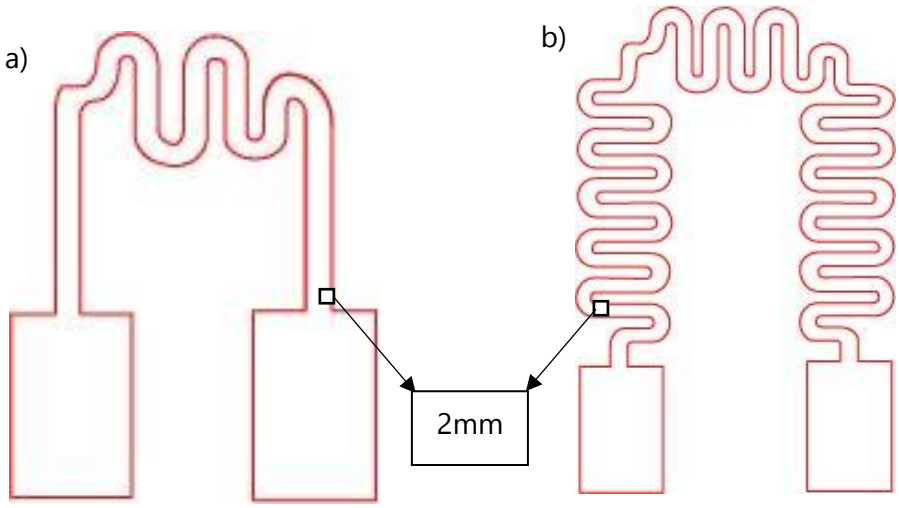

Figure 6.2 - Schematics of the subdivision of the designed sensors in 0.2 mm squares: a) simpler design; b) sensor with more complex design.

The first step is to calculate the sheet resistance for the aluminum sensors which is given by:

$$R_{s(Al)} = \frac{\rho \mathrm{Al}}{thickness} = \frac{2.8x10^{-8}(\Omega * m)}{100x10^{-9}(m)} (=) 0.28\ \Omega/\square; \quad \text{(III.1)}$$

The calculus of the resistance of sensor PI_Al A is then:

$$R_{expected} = R_{s(Al)} \left(200 - \frac{(16+2)}{2}\right) = 53.9\ \Omega; \quad \text{(III.2) b}$$

Meanwhile the expected resistance sensor PI_Al B, is calculated as shown:

$$R_{expected} = R_{s(Al)} \left(500 - \frac{(50+2)}{2}\right) = 133.7\ \Omega; \quad \text{(III.3)}$$

The calculus of the sheet resistance for the gold sensors is given by:

$$R_{s(Au)} = \frac{\rho Au}{thickness} = \frac{2.44x10^{-8}(\Omega * m)}{80x10^{-9}(m)} (=) 0.31\ \Omega\square; \quad \text{(III.4)}$$

Sensor PI_Au A and Sensor Par_Au presents the same layout and same material, so the calculated expect resistance can be applied to both. These sensors have the same number of constituents as sensor PI_Al A, being the same layout, which are 200 squares, with 16 corner squares and the 2 big pads at the bottom. Using the sheet resistance calculated for gold, the resistance of both this sensors is given by:

$$R_{expected} = R_{s(Au)}\left(200 - \frac{(16+2)}{2}\right) = 58.3\ \Omega; \quad \text{(III.5)}$$

Sensor PI_Au B, similarly to sensor PI_Al B, possesses approximately 500 squares, 50 corner squares and 2 big pads. The resistance value for sensor PI_Au B, the more complex design, with polyimide and gold, is calculated by:

$$R_{expected} = R_{s(Au)}\left(500 - \frac{(50+2)}{2}\right) = 144.6\ \Omega; \quad \text{(III.6)}$$

Annex IV. Determination of TCR with sample cooling

The measures of the TCR for the cooling of the samples were made to ensure the reproducibility, which can be achieved, because there is a similar change in the resistance with cooling and heating, and the sensor returns to similar values to the initial resistance. In figure 6.3 is shown the TCR curve for the cooling process of sensor PI_Al A. This sensor presents a cooling TCR of 0.0014 $ºC^{-1}$.

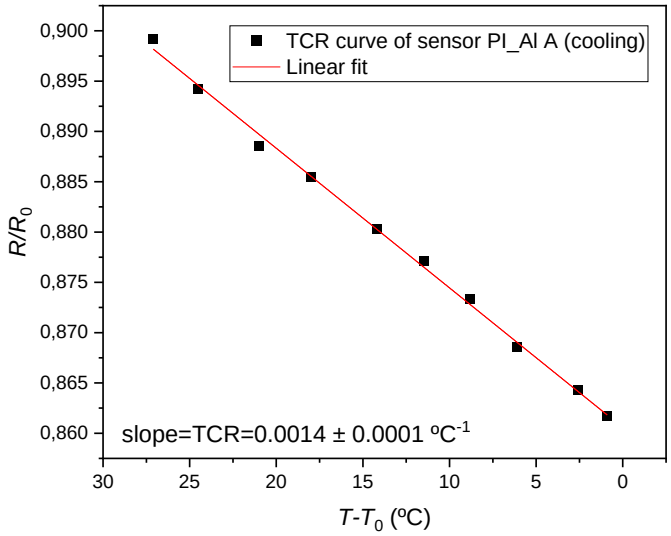

Figure 6.3 - TCR curve for the PI_Al A sensor, during cooling of the sample.

In figure 6.4 is shown, the TCR curve for the cooling of the sensor PI_Au A, and the sensor presents a cooling TCR of 0.0018 $ºC^{-1}$.

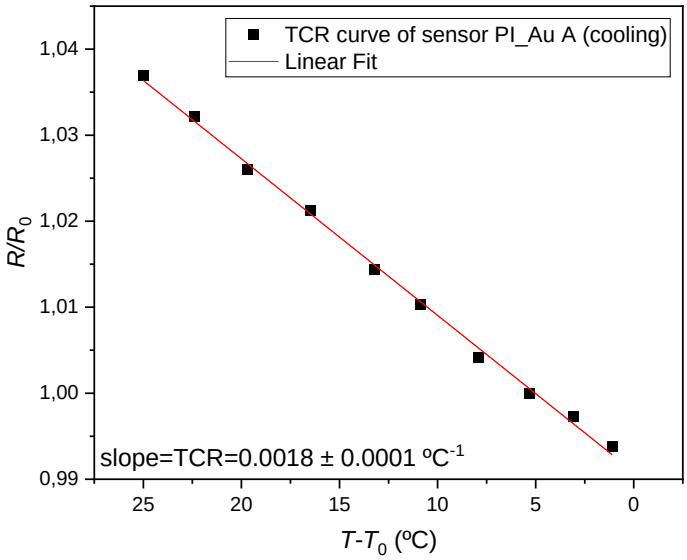

Figure 6.4 - TCR curve for the PI_Au A sensor, during cooling of the sample.

Sensor Par_Au, has the cooling TCR depicted in figure 6.5. The cooling TCR of the Par_Au sensor is 0.0013 $ºC^{-1}$.

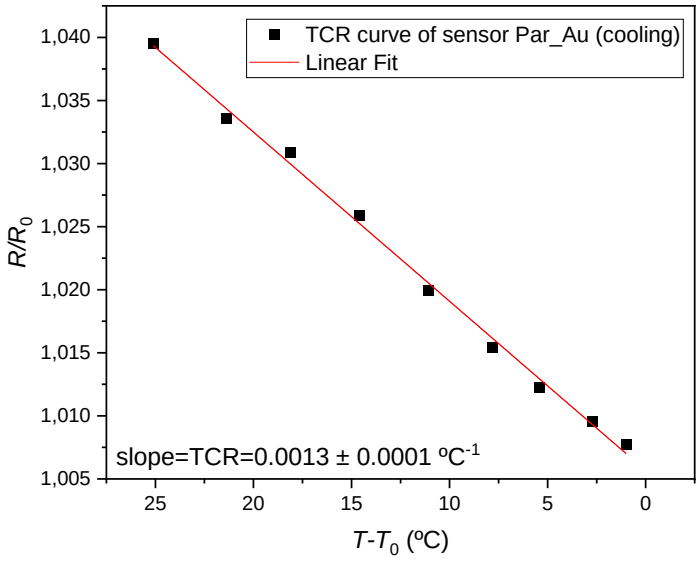

Figure 6.5 - TCR curve for the Par_Au sensor, during cooling of the sample.

Sensor PI_Au B, has the cooling TCR depicted in figure 6.6. The cooling TCR of this sensor is 0.0012 $ºC^{-1}$.

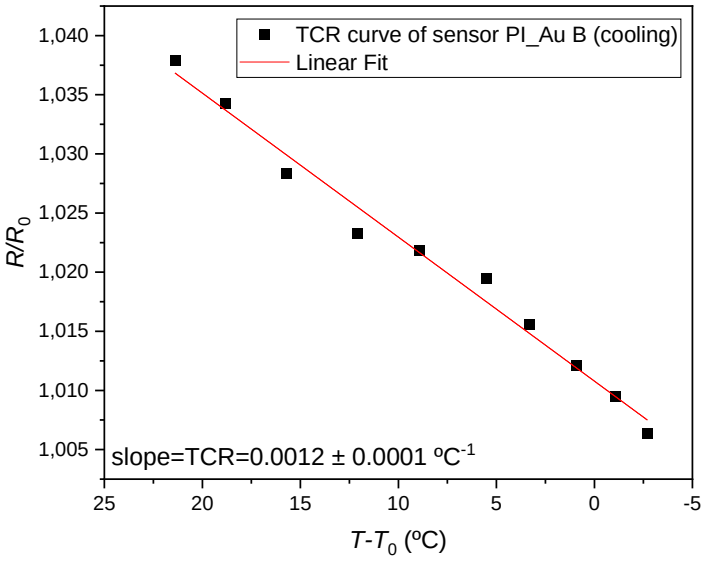

Figure 6.6 - TCR curve for the PI_Au B sensor, during cooling of the sample.

Annex V. On-skin Measurements

In figure 6.7, it is illustrated the first step, for the measurement of resistance values while the sensor is attached on-skin. In this first step, the value of resistance is measured, while the circuit is still on the tattoo paper, after the removal of the extraneous parts of the circuit. This step is made, to ensure that, both the cutting of the circuit and the removal of the extraneous parts, were performed correctly. The integrity of the circuit is then ensured, and the e-tattoo can be attached onto the skin. The sample is prepared, as illustrated in figure 6.7 a), and the measures are performed as depicted in figure 6.7 b).

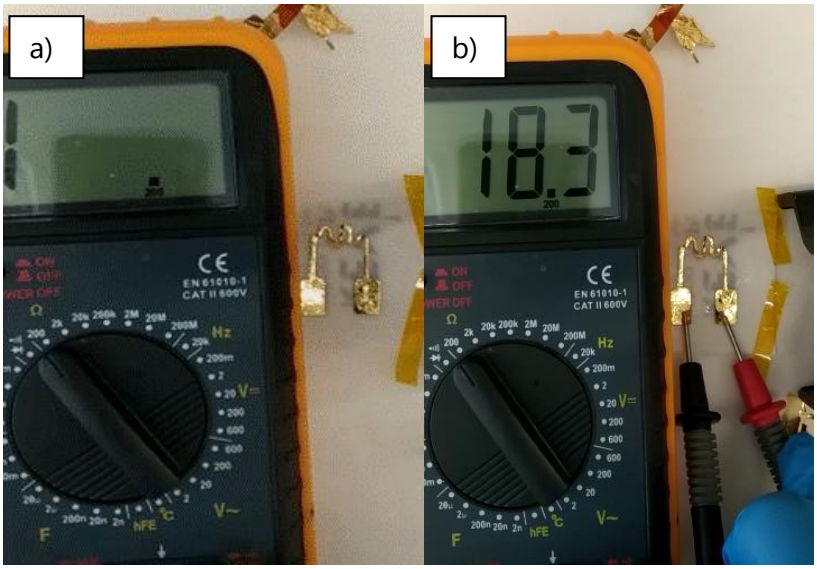

Figure 6.7 - Measurements while on the tattoo paper: a) preparation of the sample; b) measurement of resistance to confirm the integrity of the circuit.

The attachment process of the e-tattoo on the human skin is illustrated in figure 6.8. This step begins with the wetting of the tattoo paper, shown in figure 6.8 a), in order to re-dissolve the water-soluble adhesive. This allows for the removal of the tattoo paper, and the complete transfer of the circuit onto the human skin, illustrated in figure 6.8 b) below. Usually, in this step, a spray-on glue is used, in order to preserve the integrity of the circuit while on-skin.

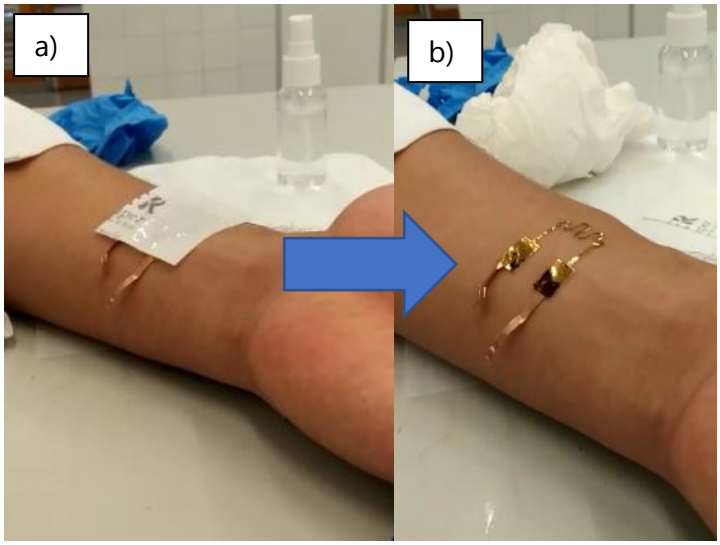

Figure 6.8 - a) Attachment of the circuit to the human skin and wetting of the tattoo paper; b) removal of the tattoo paper, leaving only the desired circuit on-skin.

Finally, in figure 6.9, the measurements on-skin are illustrated. With both previous steps correctly ensured, two alligator clips, are attached to the e-tattoo. This is possible due to the placement of copper strips in the sensor's pads.

It's important to refer that the illustrated pictures are that of different sensors, so the resistance values are merely illustrative, and don't correlate.

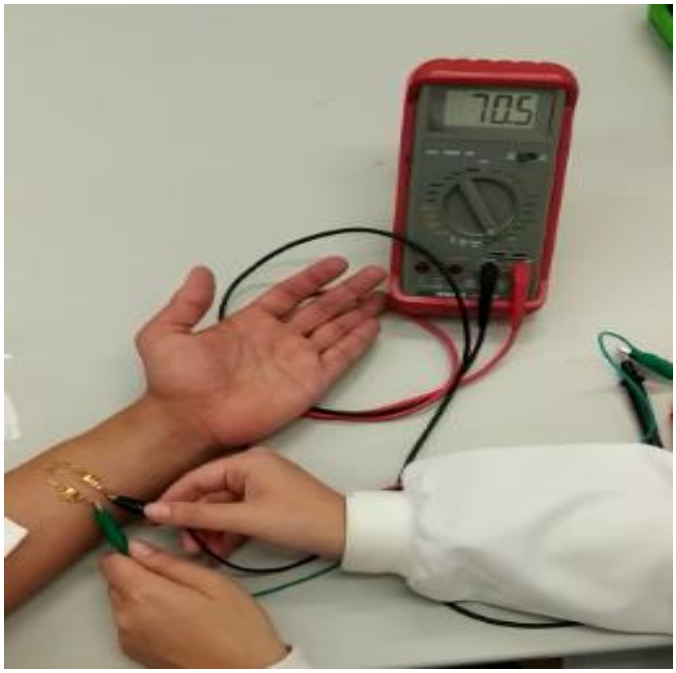

Figure 6.9 - Measurements of resistance, while the sensor is attached on-skin.